Available online at www.sciencedirect.com
SCIENCE DIRECT®
Journal of Electron Spectroscopy and Related Phenomena 150 (2006) 86–104
JOURNAL OF ELECTRON SPECTROSCOPY and Related Phenomena
www.elsevier.com/locate/elspec

Soft X-ray microscopy and spectroscopy at the molecular environmental science beamline at the Advanced Light Source

H. Bluhm[a,*], K. Andersson[b,c], T. Araki[d], K. Benzerara[e,1], G.E. Brown[b,e], J.J. Dynes[d], S. Ghosal[f,g], M.K. Gilles[a], H.-Ch. Hansen[h], J.C. Hemminger[f], A.P. Hitchcock[d], G. Ketteler[g], A.L.D. Kilcoyne[l], E. Kneedler[i], J.R. Lawrence[j], G.G. Leppard[n], J. Majzlam[k], B.S. Mun[l], S.C.B. Myneni[k], A. Nilsson[b,c], H. Ogasawara[b], D.F. Ogletree[g], K. Pecher[m], M. Salmeron[g], D.K. Shuh[a], B. Tonner[m], T. Tyliszczak[a], T. Warwick[l], T.H. Yoon[e,2]

[a] *Lawrence Berkeley National Laboratory, Chemical Sciences Division, Mail Stop 6R2100, One Cyclotron Road, Berkeley, CA 94720, USA*
[b] *Stanford Synchrotron Radiation Laboratory, Menlo Park, CA 94025, USA*
[c] *FYSIKUM, Stockholm University, Albanova University Center, S-10691 Stockholm, Sweden*
[d] *Brockhouse Institute for Materials Research, McMaster University, Hamilton, Ont., Canada, L8S 4M1*
[e] *Department of Geological and Environmental Sciences, Stanford University, Stanford, CA 94305, USA*
[f] *Department of Chemistry, University of California, Irvine, CA 92697, USA*
[g] *Materials Sciences Division, Lawrence Berkeley National Laboratory, Berkeley, CA 94720, USA*
[h] *Department of Natural Sciences, The Royal Veterinary and Agricultural University, DK 1871 Frederiksberg, Denmark*
[i] *FEI Company, Hillsboro, OR 97124, USA*
[j] *National Water Research Institute, Saskatoon, Sask., Canada S7N 3H5*
[k] *Department of Geosciences, Princeton University, Princeton, NJ 08544, USA*
[l] *Advanced Light Source, Lawrence Berkeley National Laboratory, Berkeley, CA 94720, USA*
[m] *Chemical Sciences Division, Pacific Northwest National Laboratory, Richland, WA 99352, USA*
[n] *National Water Research Institute, Burlington, Ont., Canada L7R 4A6*

Available online 10 October 2005

Abstract

We present examples of the application of synchrotron-based spectroscopies and microscopies to environmentally relevant samples. The experiments were performed at the molecular environmental science beamline (11.0.2) at the Advanced Light Source, Lawrence Berkeley National Laboratory. Examples range from the study of water monolayers on Pt(1 1 1) single crystal surfaces using X-ray emission spectroscopy and the examination of alkali halide solution/water vapor interfaces using ambient pressure photoemission spectroscopy, to the investigation of actinides, river water biofilms, Al-containing colloids and mineral–bacteria suspensions using scanning transmission X-ray spectromicroscopy. The results of our experiments show that spectroscopy and microscopy in the soft X-ray energy range are excellent tools for the investigation of environmentally relevant samples under realistic conditions, i.e., with water or water vapor present at ambient temperature.

Keywords: X-ray photoelectron spectroscopy; Scanning transmission X-ray microscopy; X-ray emission spectroscopy; Near-edge X-ray absorption fine structure; Water environmental science

1. Introduction

Molecular environmental science (MES) is an expanding field that studies, on a molecular level, chemical and biological processes occurring at environmentally relevant surfaces and interfaces. Fundamental understanding of these processes is necessary to solve important problems in environmental science related to the speciation, distribution, reactivity, transformations, mobility, and potential bioavailability of pollutants and contam-

* Corresponding author. Tel.: +1 510 486 5431; fax: +1 510 495 2067.
E-mail address: HBluhm@lbl.gov (H. Bluhm).
[1] Present address: Institut de Minéralogie et Physique de la Matière Condensée, UMR 7590 CNRS and Institut de Physique du Globe de Paris, F-75252 Paris Cedex, France.
[2] Present address: Department of Chemistry, College of Natural Science, Hanyang University, 17 Haengdang-dong, Seongdong-gu, Seoul 133–791, South Korea.

0368-2048/$ – see front matter © 2005 Elsevier B.V. All rights reserved.
doi:10.1016/j.elspec.2005.07.005

inants in the environment. Synchrotron-based spectroscopies enable the study of, e.g., aqueous solute complexes, amorphous and crystalline materials, solid/liquid, and liquid/vapor interfaces, as well as the interaction of heavy metals with biofilms and plants [1]. With the growth of the MES community, the demand for dedicated beamlines and endstations for conducting MES research has been increasing over the last decade. The MES beamline at the Advanced Light Source (ALS), Lawrence Berkeley National Laboratory, was designed with the goal of providing access for the MES community to different kinds of synchrotron-based techniques in the soft X-ray energy range (75–2150 eV), in particular scanning transmission X-ray microscopy (STXM), ambient pressure photoemission spectroscopy (PES), near-edge X-ray absorption fine structure (NEXAFS) spectroscopy, and X-ray emission spectroscopy (XES). The energy range of the MES beamline coincides with the K-edges of the most abundant elements on Earth's surface (C, N, O, Na, Mg, Al, and Si) and the L-edges of all the important transition metals (Ti, V, Cr, Mn, Fe, Co, Ni, Cu, and Zn) as well as the L-edges of P, S, Cl, K, and Ca. For the heavier elements there are other absorption edges, which can be accessed at the MES beamline. The three permanent endstations at the beamline allow investigations of samples under different environments, from UHV surface-science-type studies of well-defined surfaces, to spectromicroscopy studies of complex samples, including mixtures of inorganic solids, natural organic matter, and microorganisms under wet conditions.

One of the areas of special importance for MES is the interaction of water with surfaces, starting from the adsorption of monomers, to the formation of monolayers and eventually the presence of bulk water and its reaction with the surface [1–3]. Water plays a very important role in the distribution of contaminants and pollutants that originate from, e.g., agriculture, mining, industrial production, and radioactive waste disposal sites. Most of the chemical reactions that are important for environmental processes take place at the solid–liquid interface between water or aqueous solutions and metals, minerals, soils, and rocks. The water solubility of contaminants and pollutants also greatly influences their mobility. An important task for the MES beamline is therefore the investigation of environmentally relevant samples under "wet conditions", which is also essential for the study of biological samples that can be kept fully hydrated if they are mounted in an aqueous solution. STXM [4] is ideally suited to investigate small particles, membranes, or even cells and whole bacteria immersed in aqueous solution. Since photons have an attenuation length in liquid water on the order of several hundred nanometers at energies below and above the oxygen K-edge, imaging samples in bulk solution is possible, if the thickness of the sample is in the sub-micrometer range. STXM also allows one to obtain NEXAFS spectra with a spatial resolution of 30 nm [5], so that the chemical state and the morphology of the sample can be directly correlated. In addition to STXM, XES [6] as a photon-in-photon-out technique is well suited for studies of bulk aqueous solution samples in an atom-specific way. Ambient pressure PES [7] on the other hand, is an excellent tool for the investigation of the solution/vapor interface, where aqueous solution samples can be studied in thermodynamic equilibrium with their vapor. It is also a powerful method for studying the initial stages of water adsorption on surfaces under ambient conditions, e.g., determining the number of monolayers of water on the surface as a function of relative humidity. The combination of PES with XES and NEXAFS provides information about the electronic and geometric structures of water layers on solid surfaces, in particular the chemical bonding of water molecules to the substrate and the hydrogen bonding network within the water layer [8].

Another area of special importance to MES is the investigation of radioactive materials, in particular actinides, to understand the sequestration of these materials in complex natural environments. STXM offers the opportunity to investigate radioactive samples in an efficient and safe way, since the amount of material that is needed in the experiments is on the order of only 10 fg.

In the following section, we discuss the setup and properties of the beamline and the dedicated endstations. In the main part of the manuscript, we present examples for the application of synchrotron-based soft X-ray spectroscopy and microscopy to the study of environmental materials and processes. The examples cover a wide range of MES research, among them fundamental studies of well-defined adsorbate layers on single crystalline surfaces under ultra-high vacuum conditions, alkali halide solutions in the presence of water vapor, uranium oxide particles, as well as biofilms, bacterial-mineral samples, and aluminum flocs in aqueous solutions.

2. Description of experimental facilities

2.1. Beamline

The design and the properties of the ALS-MES beamline 11.0.2 will be explained in detail in a forthcoming paper. Here, we describe the main design features of the beamline in brief. A schematic overview of the main beamline components is shown in Fig. 1. The MES beamline uses photons from an elliptically polarizing undulator with a 5 cm period [9]. With the Advanced Light Source operating at an energy of 1.9 GeV it provides photons in the energy range from 75 to 2150 eV. The photons from the undulator are focused vertically by a sagittal cylinder mirror onto the pre-mirror of a SX700 style plane-grating monochromator [9–11]. There is no entrance slit in front of the monochromator. The monochromator is equipped with two gratings (150 and 1200 lines/mm). The whole monochromator tank is moved when the gratings are changed. The light from the monochromator is focused by either of two toroidal focus mirrors that generate a stigmatic focus at the exit slits of either the STXM or the spectroscopy branch line. The branch line is selected by the position of the spectroscopy mirror either in or out of the beam path. The exit slits are illumination sources for the zone plate of the STXM, or a pair of Kirkpatrick–Baez (KB) mirrors in the spectroscopy branch line. The KB mirrors (horizontal and vertical) are able to focus the spot in the experimental chambers down to 7 μm × 10 μm.

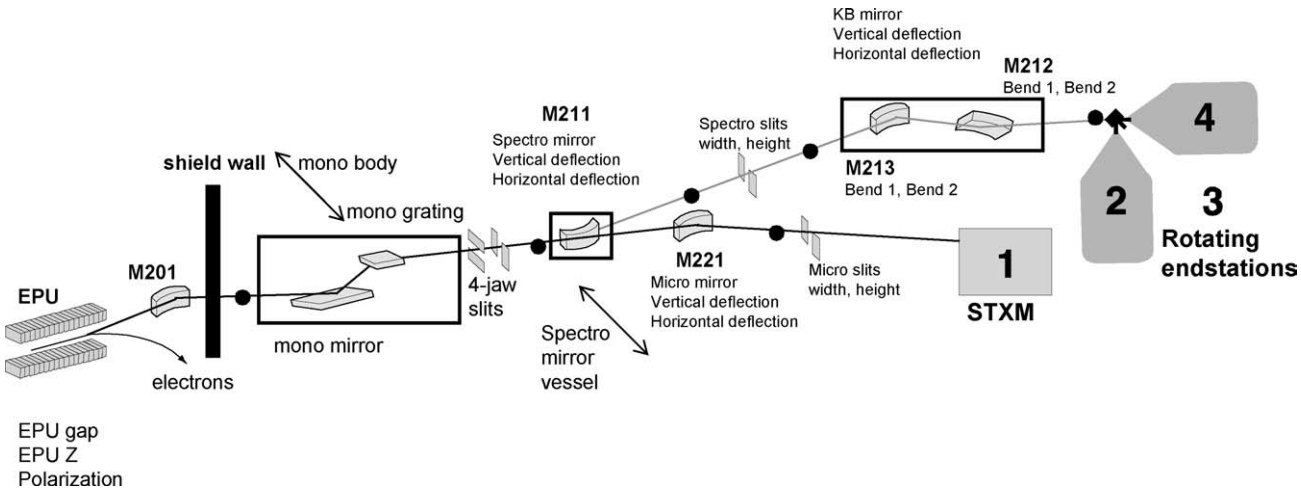

Fig. 1. Schematic layout of the MES beamline (11.02.) at the Advanced Light Source (for details see text).

The beamline features three dedicated endstations. While the STXM is permanently installed at its dedicated branch line, the two spectroscopy chambers (ambient pressure photoemission and wet spectroscopy endstation) are mounted on platforms that can be moved on air bearings. The endstations can be switched between the on-beam and off-beam positions in about 30 min without breaking vacuum. External user endstations can be mounted on a separate platform that can then be brought into the on-beam position. The three dedicated endstations are described in the following section.

2.2. Scanning transmission X-ray microscope (STXM)

The STXM endstation [4] is located on the optimized microscopy branch line in an isolated area (see Fig. 1). Photons are admitted to the STXM chamber through a silicon nitride window. The photon beam is focused onto the sample by a zone plate with a working distance of 0.5–9 mm, depending on photon energy. An order-selecting aperture (OSA) is placed between the zone plate and the sample. The sample is scanned relative to the focused X-ray beam, and the transmitted intensity is recorded as a function of sample position using a photomultiplier tube or a photodiode. The zone plate can focus the beam down to a spot size of 25 nm, for a maximum spatial resolution of 30 nm. Several different zone plates are used depending on photon energy, required spatial resolution and minimum working distance. The maximum energy resolution $E/\Delta E$ is better than 7500, and a resolution better than 3000 is achieved at a photon flux of 10^8–10^9 s^{-1} in the sub-50 nm focused beam at energies of about 200–1600 eV. The maximum raster scan range is 20 mm × 4 mm, while the minimum step size is 2.5 nm. Images with up to 3000 × 2000 pixels can be acquired at any spatial size regime meeting these limits. The very wide dynamic range of the spatial scanning system, achieved with continuous interferometric feedback of positioning with an accuracy of 5 nm is a very powerful aspect of the MES STXM. The available energy range is 90–2150 eV. Typical dwell times per pixel are 0.1–1.0 ms.

2.3. Ambient pressure photoemission spectroscopy (APPES) endstation

The ambient pressure photoemission spectrometer allows investigation of samples at pressures of up to 10 Torr. The key part of the spectrometer is a differentially pumped electrostatic lens system that separates the sample chamber from the hemispherical electron analyzer (Phoibos 150, Specs). The principle of this type of spectrometer is described in Ref. [7]. Incident X-rays from the beamline are admitted to the ambient pressure cell through a silicon nitride window (thickness 100 nm, active window area 1 mm × 1 mm). The sample is placed at a distance of ∼0.5 mm from an aperture with 0.3 mm diameter, which is the entrance to the differentially pumped lens system. Electrons and gas molecules escape through this aperture into the differentially pumped lens system. The electrons are focused in the first differential pumping stage onto a second aperture (diameter 2 mm), and in the second differential stage onto a third aperture, also with a 2 mm diameter, before entering a final lens stage and being eventually focused onto the entrance slit of the hemispherical analyzer. The pressure differential between the ambient pressure cell and the hemisphere is about eight orders of magnitude.

For the investigation of samples in a controlled humidity atmosphere up to the condensation point of water, the sample surface has to be the coldest point in the chamber. We have developed a transferable sample holder cooled by a two-stage Peltier element, which is isolated from the chamber atmosphere [12]. This sample holder, combined with a stand-alone chiller for temperature control of the sample holder docking station, which acts as a heat sink for the hot side of the Peltier element, allows control of the sample temperature from 220 to 350 K. For surface-science-type experiments, a button heater combined with liquid nitrogen cooling provides a temperature range from 100 to 1000 K.

Besides the ambient pressure cell, the ambient pressure PES endstation has a preparation chamber which is equipped with a sputter gun and a plasma source for sample cleaning, and a com-

bined LEED/Auger instrument for characterization of samples. A load-lock chamber allows fast exchange of samples.

2.4. Wet spectroscopy endstation (WES)

The wet spectroscopy endstation features a fast load-lock, a preparation chamber, and a spectroscopy chamber. The preparation chamber is equipped with a plasma source and a sputter gun for sample cleaning, and a LEED/Auger system for sample characterization. In the spectroscopy chamber, a Scienta SES100 analyzer is used for photoemission spectroscopy, and a soft X-ray emission spectrograph that was developed at the Advanced Light Source [13,14] is used for X-ray emission spectroscopy. The sample temperature can be varied from 10 to 1400 K. The WES endstation is currently used mainly for studies under ultra-high vacuum conditions, but it will be outfitted with an environmental cell for photon in-photon out studies on liquids or at elevated pressures in the near future.

3. Results and discussion

In the following, we present recent data from experiments that were either performed at the MES beamline or that exemplify the types of research that will be done in the near future on this beamline. We start with studies on the basic interaction of water with single-crystal metal surfaces, then describe measurements of ions at the solution/vapor interface, and afterwards discuss the application of STXM to the investigation of actinides, minerals, biofilms, and mineral–bacteria suspensions.

3.1. Chemical bonds at surfaces and interfaces probed with X-ray emission spectroscopy (H. Ogasawara, K. Andersson, A. Nilsson)

Most of the important chemical reactions related to environmental processes take place at surfaces and interfaces. If we can understand how chemical bonds are formed and transformed on surfaces during a chemical reaction, it will be possible to control and modify these processes. There are, however, a large number of atoms involved in these processes at the interface and it has been an experimental challenge to obtain atom-specific information on surface chemical bonds.

X-ray emission spectroscopy (XES) has the unique ability to provide *an atom-specific probe of chemical bonds* [6]. It allows us to spotlight one specific atom on the surface at a time. Fig. 2 illustrates the X-ray emission process for an adsorbed N_2 molecule on a surface. The atomic sensitivity arises because the core hole created in the nitrogen K-edge absorption process is filled only by valence electrons in the proximity of the excited atom. The valence electronic structure is projected on a specific atom. XES is therefore an experimental analog of the linear combination of atomic orbitals (LCAO) approach for molecular orbital theory. Furthermore, the chemical shift in the N 1s core level allows a selective probing of the two inequivalent nitrogen atoms [15].

We can now study how molecular orbitals of a specific symmetry are distributed over different atomic sites in a complicated

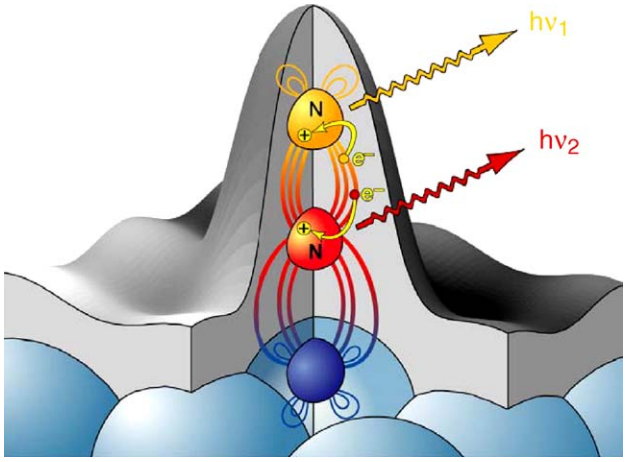

Fig. 2. Schematic picture illustrating the local probe character in XES for N_2 adsorbed on a surface. From the total charge density (gray envelope) valence electrons with p-angular momentum (contour lines) decay into the N 1s core hole.

molecular adsorption complex. Fig. 3 shows the polarization dependent X-ray emission O, C, and N spectra of glycinate adsorbed on Cu(1 1 0) [16]. These data were measured at beamline 8.0 at the Advanced Light Source in Berkeley. Upon adsorption of the amino acid glycine on Cu(1 1 0), the amino group remains intact whereas the acidic hydrogen on the carboxyl group is removed, leaving behind adsorbed glycinate. While the tunability of the incident photon energy is used to select a specific atom of glycinate by its core binding energy, the polarization of the emitted radiation provides directional sensitivity to the bonding. The molecule is oriented perpendicular to the Cu rows on the two-fold symmetric surface allowing for projection of the $2p_x$, $2p_y$ and $2p_z$ valence orbitals by means of orientation dependent studies. Combined with theoretical calculations, details in the surface chemical bonding can be obtained from such studies. It is shown that the electronic structures of these functional groups are affected not only by the surface but also by hydrogen bonding to neighboring molecules.

Recently, an X-ray emission spectroscopy study of a water monolayer showed how water molecules are bound to Pt(1 1 1) [8]. Water molecules adsorb intact on Pt(1 1 1) and form an in-plane two-dimensional hexagonal hydrogen bond network. In the layer, water molecules are alternately bonding to the surface through either oxygen or hydrogen atoms. X-ray emission spectra for oxygen-bonding or hydrogen-bonding water were recorded in a site-specific way by tuning the photon energy of excitation (Fig. 4). The bonding mechanism shown in the insert is proposed based on the analysis of spectral features in XES combined with the electronic structure calculations [8].

Under some circumstances, adsorbed water decomposes, splitting one of the internal O–H bonds to produce adsorbed hydroxyl and hydrogen as depicted assuming the potential energy diagram shown in Fig. 5. There is an activation barrier that kinetically hinders the decomposition of water. This kinetic barrier can be overcome if sufficient thermal energy, e.g., temperature, pressure, is added to the system. On Ru(0 0 1), a dissociated layer is thermodynamically favorable, however it is

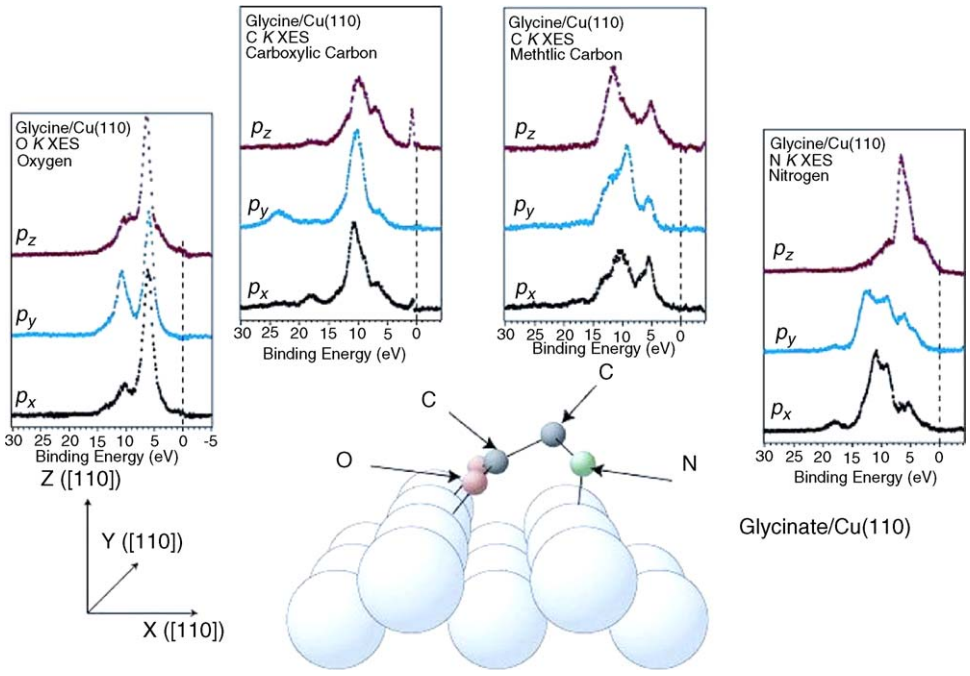

Fig. 3. Molecular adsorption structure of glycinate adsorbed on Cu(1 1 0) with XES spectra measured in three directions on all four C, N, and O atomic centers (taken from Hasselstrom et al. [16]).

not observed at 150 K (Fig. 5) [17]. To overcome the kinetic barrier for dissociation it is necessary to introduce water at temperatures above the desorption temperature of the intact layer of 160 K. This result demonstrates the importance of studying the solid–water interface under various thermodynamic conditions, since there are wide ranges of thermal and pressure conditions encountered in nature, producing various phases of water layers with different physical and chemical properties.

3.2. Vapor-solution interface probed with ambient pressure photoemission spectroscopy (S. Ghosal, J.C. Hemminger, H. Bluhm, B.S. Mun, G. Ketteler, D.F. Ogletree, M. Salmeron)

The interfaces of aqueous solutions are playing an important role in atmospheric and environmental chemistry. An important question is the concentration of ions at the solution/vapor interface, since this has a strong influence on reaction rates between gas phase molecules and the ions in the solution. The conventional view, until recently, was that the vapor/solution interface is devoid of ions due to image charge repulsion [18]. The observed reaction rates between alkali-halide salt solutions and gaseous Cl_2 and Br_2 however indicate that Cl^- and Br^- ions exist at the interface of the solution [19,20]. Non-linear optical spectroscopy experiments have also inferred the existence of anions close to the interface of salt solutions [21–23]. In addition, molecular dynamics simulations for 1.2 M sodium halide solutions have predicted that large, polarizable anions, such as Br^- and I^-, segregate to the surface, while the sodium ions remain in the bulk of the solution, essentially forming an electric double layer at the solution–vapor interface [24,25]. Previously X-ray photoemis-

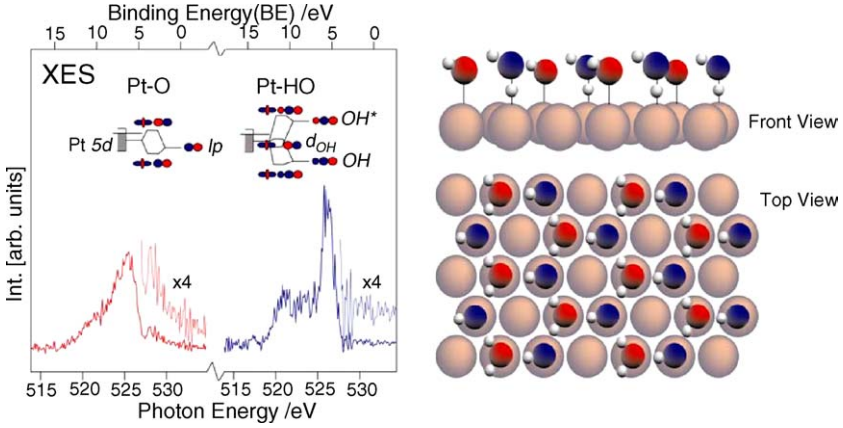

Fig. 4. Schematic view of water adsorbed on Pt(1 1 1) taken from Ogasawara et al. [4] showing water species O-bonding (red) and H-bonding (blue) to Pt(1 1 1) with their corresponding XES spectra. The hydrogen atoms (white) connects the water molecules in the hydrogen bonding network but also connects the H-bonding water species (blue) to the surface.

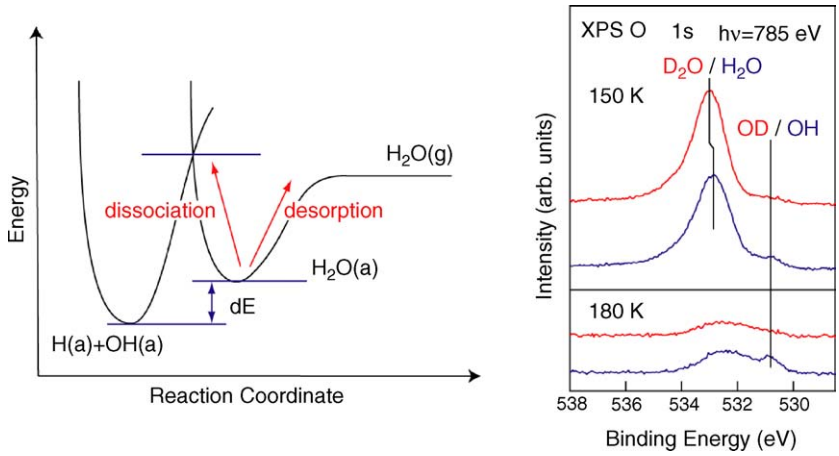

Fig. 5. O 1s XPS for water (H_2O and D_2O) adsorbed on Ru(0 0 1) taken from Andersson et al. [17]. Chemical species on Ru(0 0 1) are identified with chemical shifts in the O 1s XPS. The formation of hydroxyl at 180 K is characterized by the appearance of O 1s XPS peak at ca. 531 eV, whereas that for intact water appears at ca. 532–533 eV. The decomposition is observed for H_2O but not for D_2O due to zero point energy differences.

sion spectroscopy had been shown by Siegbahn and co-workers to be an excellent tool for the measurement of ionic segrgation at the liquid/vapor interface [26–28].

We have used ambient pressure PES to directly measure the ion concentration at the vapor/solution interface of potassium halide solutions. KBr and KI single crystals were cleaved inside the vacuum chamber, or directly before introduction to the vacuum chamber. The crystals were then exposed to water vapor at a pressure of 1.5 Torr. The relative humidity (RH) at the sample surface was controlled by changing the sample temperature. When a salt sample is exposed to water vapor, at a certain humidity it reaches its deliquescence point where the solid salt, water vapor, and a layer of saturated solution on the salt surface are in equilibrium. For KBr and KI the deliquescence point is reached for a RH of 81 and 75%, respectively. Care has to be taken in the experiments to minimize the exposure of the sample surface to the intense incident photon beam, since this can lead to the depletion of mainly the halide ions at the sample surface. Each spectrum was therefore taken at a new sample location to minimize radiation damage.

From the results of the molecular dynamics simulations it is expected that for a KBr or KI solution the anion/cation stoichiometry deviates from the bulk value of 1 in favor of the anion at the solution/vapor interface. The results of our photoemission experiments for the case of a KBr crystal are shown in Fig. 6 [29]. All spectra were measured at the same kinetic energy (160 eV), which assures that the effects of scattering of electrons by gas molecules are the same for both K 3p and Br 3d photoelectrons, and that contributions from the lens transmission function cancel out. The spectra were normalized by the incident photon flux which was measured using a calibrated photo diode, and by the photoemission cross-section [30]. The Br/K ratio remains constant around an average value of 0.8 ± 0.1 during the increase of the relative humidity to just below the deliquescence point. However, at the deliquescence point, when a visible droplet of KBr solution is formed at the KBr surface, the Br/K ratio increases to 2.5 ± 0.2. A similar change was also observed in the case of KI (data not shown), where the K/I ratio increased

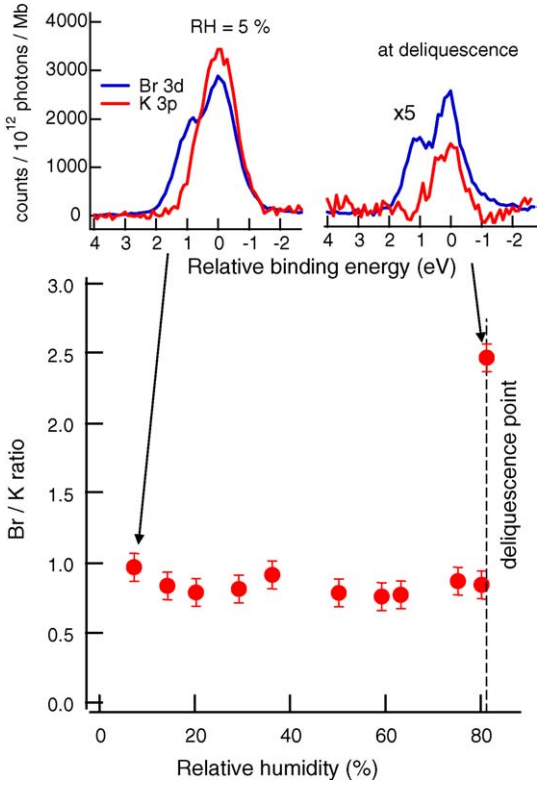

Fig. 6. Bromine-to-potassium ratio as a function of relative humidity for a KBr(1 0 0) surface. The Br 3d and K 3p photoemission spectra for RH 5% and at the deliquescence point are also shown. All spectra were taken for a kinetic energy of 160 eV and are normalized for incident photon flux and photoemission cross-section, so that the peak areas of the Br 3d and K 3p spectra can be compared directly. At 5% RH the Br/K ratio shows the expected value of 1.0 ± 0.1 and does not change significantly, until the deliquescence point is reached. At deliquescence the Br/K ratio shows a strong increase to a value of 2.5 ± 0.1. The intensity of the spectra at deliquescence is multiplied by a factor of 5. The attenuation of the Br 3d and K 3p signal is due to the adsorption of water at the surface.

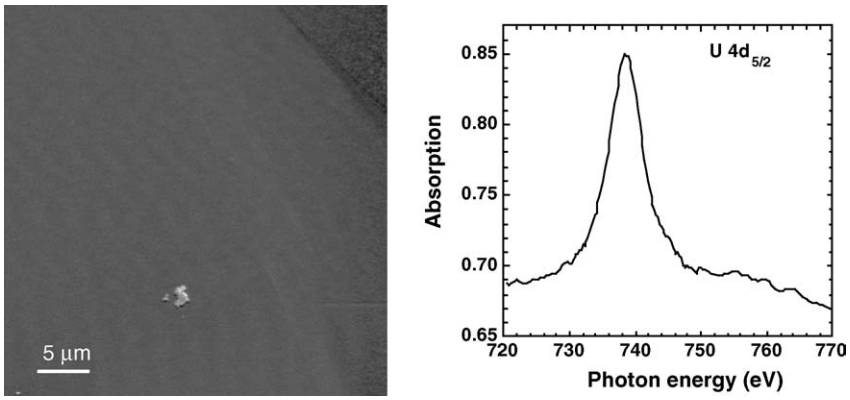

Fig. 7. Normal absorption contrast image obtained at approximately 700 eV of UO_2 particles (left panel) and the NEXAFS spectrum collected at the U $4d_{5/2}$ edge from a 35 nm edge region of one of the particles (right panel).

from 1 below the deliquescence point to 3.4 at the deliquescence point. Measurements of the absolute atomic concentration in the interface region from the Br 3d (and I 4d, respectively), K 3p and O 1s spectra showed that the concentration of both bromine and iodine ions at the interface is enhanced by at least a factor of 2.5 compared to the expected value in the absence of ion segregation at −10 °C (Br/K/O(H_2O) = 5.5:5.5:89, and I/K/O(H_2O) = 10:10:80 [31]). These findings prove that anions are present at the solution/vapor interface and therefore are likely participants in chemical reactions between gas molecules and solution ions. We should note that in carrying out experiments on solution interfaces, it is impossible to completely avoid contamination of the interface with impurities. In our experiments, the liquid/vapor interface contains small amounts (sub-monolayer) of carbonaceous material. The anion/cation ratios that we measure are insensitive to these amounts of carbon at the interface.

Our present study was limited to saturated solutions; it will be important to investigate the absolute concentration of ions at the solution/vapor interface at lower bulk concentrations. In addition, we will study the influence of carbonaceous materials, which will always be present under realistic conditions at the interface, on the properties of solution/vapor interfaces.

3.3. Scanning transmission X-ray microscopy of uranium oxide particles (T. Tyliszczak, D.K. Shuh)

The emergence of microspectroscopic and fluorescence-based techniques has permitted investigations of actinide materials at sources of soft X-ray synchrotron radiation [32–34]. Spectroscopic techniques with fluorescence-based detection are particularly useful and have immediate utility for actinide investigations since they are sensitive to small amounts of material, can be bulk or surface sensitive, thereby avoiding complications of clean surface preparation and the associated safety considerations. However, the use of spectromicroscopy to investigate prototypical uranium oxide particulates in the ALS-MES beamline STXM has been a recent development. The performance characteristics of the ALS-MES STXM permit spatial imaging with a resolution of approximately 30 nm and NEXAFS spectroscopy with a tunable energy resolution of better than 7500 [4,35].

Soft X-ray STXM is potentially well suited for the investigation of actinide or other radioactive materials since the amount of material required is conservatively estimated to be on the order of 10 fg for a particle. This simplifies safety considerations since the corresponding total activity would be well below a picocurie (pCi) if a single particle could be successfully isolated and mounted in the STXM sample holder for even the most radioactive of the common actinide nuclides. The radioactive material can be safely and permanently enclosed between two 50 nm thick silicon nitride windows to form a sample package suitable for STXM experiments. In practice, multiple particles are dispersed within the silicon nitride sample package. The overall safety envelope of the radioactive STXM experiments is further enhanced since the ALS-MES STXM end station is isolated from the ALS storage ring vacuum by a silicon nitride window, which permits the operation of the STXM under an ambient helium atmosphere, thereby avoiding problems that might arise from the exposure of the sample package to a vacuum. A prerequisite for STXM samples is that they have an accessible thickness of a few hundred nanometers depending on the elemental cross-section, energy of the absorption edge, and local elemental concentration.

The actinide elements have several electron core levels that reside in the soft X-ray energy regime. The most well known of these actinide element thresholds are the $5d_{5/2,3/2}$ that lie in the range of 90–150 eV for the lighter actinides and have giant cross-sections [36]. These are similar to the giant resonances of the lanthanide element $4d_{5/2,3/2}$ edges that are also found in approximately the same energy range but extend to higher energies as the lanthanide period is traversed. However, the strong absorption in the silicon nitride windows at about 100 eV (Si L-edge) limits the usefulness of the STXM around this energy. The routine energy range for samples enclosed in silicon nitride windows is therefore 130–2150 eV. For uranium, this includes the entire $N_{I–VII}$ edge series (4s, $4p_{1/2,3/2}$, $4d_{3/2,5/2}$, $4f_{5/2,7/2}$).

Uranium oxide of nominal composition $^{238}UO_2$ (Alfa Aesar, Johnson Matthey) was ground into a powder. The resulting particles were dispersed onto a 50 nm silicon nitride window in the Heavy Element Research Laboratory of LBNL. A second 50 nm window was epoxied and sealed to the first and the sample package transported to the ALS in accordance with

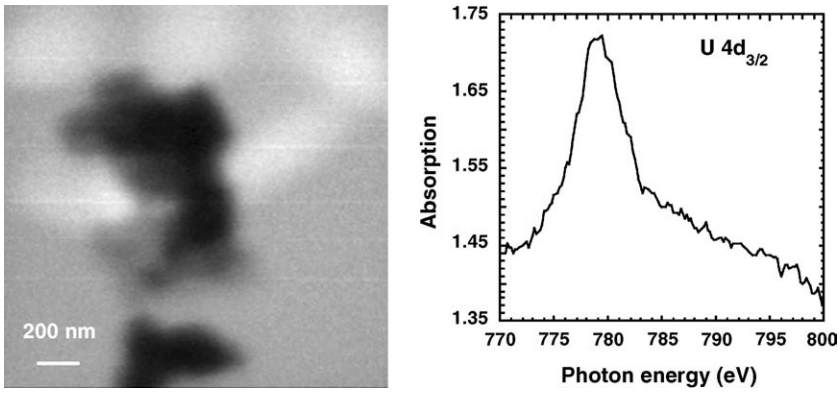

Fig. 8. Higher magnification normal absorption contrast image obtained at approximately 700 eV of the UO_2 particles shown in Fig. 1 (left panel) and the NEXAFS spectrum collected at the U $4d_{3/2}$ edge from a 35 nm edge region of one of the particles (right panel).

ALS/LBNL radioactive materials handling protocols. Radioactive sample package holders were handled, loaded, unloaded, and the ALS-MES STXM certified as non-radioactive following the completion of the experiments under the supervision of a LBNL radiological control technician. All images and NEXAFS spectra were recorded with the ALS-MES beamline elliptical polarization undulator in the horizontal mode.

The left panel of Fig. 7 shows a wide field image obtained of the first radioactive UO_2 particles examined at the ALS-MES STXM. Higher spatial resolution images were collected and used to select appropriate regions for NEXAFS measurements. Examination of each respective U $N_{I–VII}$ electron energy level showed that the useable absorption edges for the STXM were the U $4d_{5/2,3/2}$ thresholds. The right panel of Fig. 7 presents a U $4d_{5/2}$ NEXAFS spectrum obtained from a single scan in the line scan mode from an edge region of the UO_2 particle that was subsequently normalized to a region of the sample that had no uranium response. A higher magnification image of a different UO_2 particle is displayed in the left panel of Fig. 8 along with the corresponding U $4d_{3/2}$ NEXAFS spectrum that was collected in the same manner as its spin-orbit partner in Fig. 7. The resolution for the spectra collected in this investigation was estimated at ∼5000 based on the slit widths employed.

One noticeable feature common to both NEXAFS spectra at the U 4d edges is the large overall width of the absorption feature (∼6 eV). This broadening results from known core–hole lifetime effects at these edges. Although the broadening has little effect on the imaging quality of the STXM, a key aspect of the STXM is the capability to extract chemical information from the spectroscopy so that chemical state mapping can be performed, not just elemental mapping. Preliminary investigations of the other common uranium oxides, U_3O_8 and UO_3, at the U $4d_{5/2}$ edge have yielded small but reproducible charge state shifts from UO_2 (735.1 eV) towards higher energy of 0.9 and 1.1 eV, respectively [37]. Although the shifts are small and may not be as useful as one might have desired, they provide a much needed, critical analytical tool for determining the oxidation state of actinide materials at the tens of nanometers level. Additional, recent STXM investigations of non-oxide based uranium systems have also shown that the U charge state shifts provide a useful and reliable method for ascertaining oxidation states by U $4d_{5/2}$ edge NEXAFS [38]. During these investigations, there was no evidence for sample radiation damage.The oxides of the actinide elements are currently of great scientific interest and are of critical technological importance; thus, the ability to successfully probe the oxygen K-edge as a function of spatial position would provide a new and unique method to study these materials [39]. The oxygen K-edge NEXAFS spectrum collected by STXM spectromicroscopy techniques from the UO_2 sample are shown in Fig. 9. The NEXAFS spectrum obtained is similar to those obtained from regular NEXAFS methods of well-characterized UO_2 [40]. There were variations in the oxygen K-edge spectrum as a function of position on the UO_2 particle. As NEXAFS spectra were frequently measured at or near the particle surface to obtain a proper thickness for the oxygen absorption measurements, there may have been thickness effects that made normalization difficult or slight stoichiometry differences that both could have induced some amplitude changes in the spectra. Oxygen K-edge spectra have also recently been obtained from the common uranium oxides, U_3O_8 and UO_3, and clear differences between the spectra, similar to those observed in bulk NEXAFS spectra, are observed [41].

The initial actinide measurements employing the ALS-MES STXM demonstrate the usefulness and promise of soft X-ray

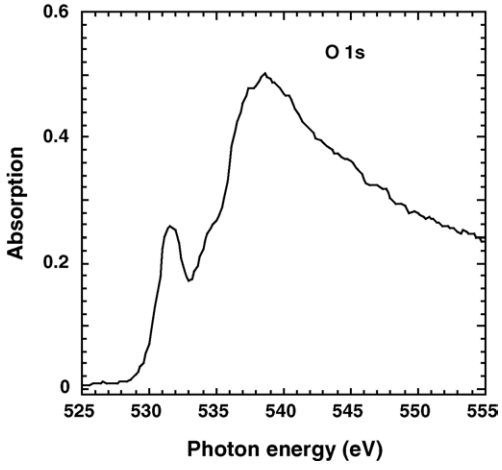

Fig. 9. Oxygen K-edge transmission NEXAFS spectrum collected from the UO_2 particle.

STXM spectromicroscopy for the investigation of actinide-related science. The operational characteristics of STXM permit the safe handling of the radioactive materials from an experimental perspective on the floor of the ALS and simplify sample preparation as well. It is envisioned that the solid state studies may be extended to actinide sample packages containing wet pastes or perhaps even liquids. From these initial results it appears that reliable chemical information can be obtained from STXM NEXAFS measurements at the actinide $4d_{5/2}$ edge, albeit the energy shifts between oxidation states is small for uranium. The actinide N-series edges, other than the 4d's, do not have sufficient photoabsorption cross-sections to be utilized in conjunction with STXM based on the response of the corresponding uranium edges. Of particular importance is the capability of the ALS-MES STXM to probe the K-edges of the lighter elements such as C, N, and O that have deterministic influences on the chemistry of actinides. Similarly, the energy resolution and sensitivity to the transition metal L-edges, present an opportunity to understand further the actinide–transition metal/transition metal oxide interactions. Combined with the nanometer spatial resolution characteristics, the spectroscopic versatility of ALS-MES STXM offers a unique tool to investigate the chemistry of actinide species in colloids, particulates, biological materials, microorganisms, the heaviest actinides, actinide chemical reactions at specific surfaces including oxides at the nanoscopic level, and in an array of additional actinide systems from which one may develop a further understanding of 5f element chemistry.

3.4. Charge state distribution of iron in synthetic green rusts (K. Pecher, H.-Ch. Hansen, E. Kneedler, B. Tonner)

Green Rust is the name for a class of mixed valent iron compounds that recently became known for being strong reducing agents for organic as well as inorganic pollutants in anoxic environmental compartments. Their crystallographic structure is defined by brucite-like sheets of Fe(II) and Fe(III) octahedrons being intercalated by charge compensating anions and water molecules [42]. Different forms of green rust with a wide range of Fe(II)/Fe(III) ratios and interlayer spacings have been identified mainly depending on anions used during synthesis or anions being present in soil or sediment pore waters [43]. To date rather incomplete information is available on the electronic structure of such compounds.

We have determined the sub-micron distribution of charge states of iron in single platelets of sulfate green rust using STXM. Mapping of the Fe(II)/Fe(III) ratio of a single hexagonal platelet of SO_4-green rust revealed considerable heterogeneity and deviation from the expected ratio of Fe(II):Fe(III) of 2 in this type of green rust, especially near the particle edges, where Fe(III) dominates (see Fig. 10). Contrary to magnetite (Fe_3O_4), NEXAFS extracted from different areas of the sample could be fitted by a linear combination of single valent model spectra.

This gives first evidence for a unique electronic structure of green rust, where formal charge states of the iron cations are not smeared out by electron delocalization like in large single crystal magnetite. It might also shed some light on preferred reaction sites on green rusts and indicates that reaction mechanisms derived from bulk stoichiometry might be too simplistic.

3.5. Structure and chemistry of Al-rich precipitates from acid environments (J. Majzlan, S.C.B. Myneni)

Acidification of natural systems caused by anthropogenic activities is a serious environmental problem. The anthropogenic sources of acidity are two-fold: acidic rain caused by the condensation of air-borne SO_2 and NO_x pollution, and acid mine drainage caused by the weathering of sulfidic minerals (mostly pyrite, FeS_2). These acidic solutions interact with minerals, organic compounds, and biota, and significantly impact various biogeochemical processes in the environment. One of the components commonly found in acidic waters is aluminum, a principal constituent of many rock-forming minerals, such as feldspars, micas, and clays. Although Al is highly toxic to biota in certain forms, such as aqueous $[Al(H_2O)_6]^{3+}$, its speciation in acidic environments and the influencing environmental variables are not well understood.

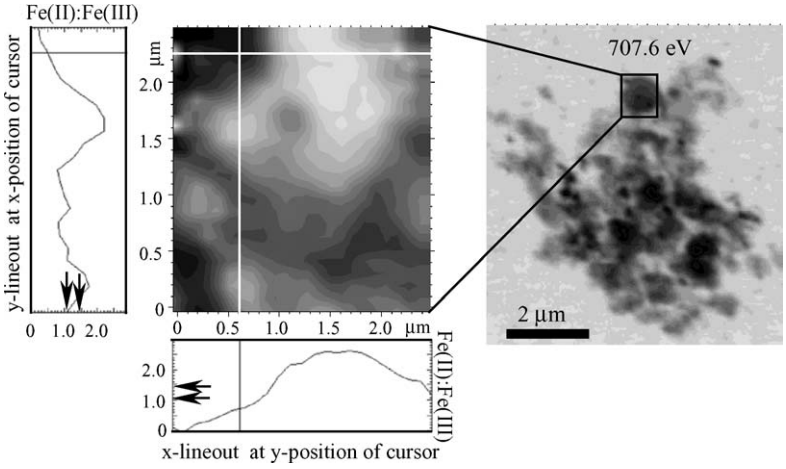

Fig. 10. Spatial distribution of Fe(II)/Fe(III) ratio in a single particle of SO_4-green rust. The *x*- and *y*-lineout plots are along the respective lines in the charge state ratio plot. The arrows correspond to the charge state ratios fitted from area averaged L-edge Fe NEXAFS.

In this study, we have investigated the aqueous solution and solid phase speciation of aluminum in the presence of different co- and counter-ions, which are common in acidic natural environments. Although previous studies (e.g., Refs. [44,45]) analyzed the Al precipitates (gels) using X-ray diffraction (XRD), these studies were limited to the bulk speciation of dry samples. While nuclear magnetic resonance (NMR) spectroscopy is a versatile technique for studying the coordination environment of Al-precipitates [46], it is difficult to examine variations in the coordination of Al using this technique. We are employing NEXAFS at the Al K-edge, and X-ray spectromicroscopy to understand the speciation of Al in solid phases, and the morphology and chemical heterogeneity of the precipitates. We are also complementing these studies with attenuated total reflectance Fourier-transform infrared (ATR-FTIR) spectroscopy, XRD and NMR. The X-ray spectromicroscopy and Al NEXAFS spectroscopy studies were conducted at the ALS-MES beamline. The XRD patterns were collected on a Scintag PAD V diffractometer with Cu Kα radiation. The ATR-FTIR spectra were collected with a Bruker IFS 66 V/s FTIR spectrometer. In all cases, the gels were analyzed without drying, in contrast to all previous studies.

Aluminum gels were synthesized by titrating solutions of $AlCl_3$, $Al(NO_3)_3$, or $Al_2(SO_4)_3$ (all 0.5 M Al) by 2 M KOH or NaOH solutions to a pH value between 3.5 and 5.5. The gels were aged for 2 weeks in the solution from which they were precipitated. During the ageing, pH values dropped slightly. The gels were either separated from their solution by centrifugation (for XRD and FTIR), or used with their solution (NEXAFS). Natural Al-oxyhydroxide and -sulfate samples were also collected at a discharge of an abandoned anthracite mine (around Tamaqua, PA) and analyzed using NEXAFS spectroscopy. The acidic discharge at this site is treated by limestone gravel, which precipitates abundant iron and aluminum-rich flocs. These flocs cover the limestone gravel as well as aquatic flora. The samples investigated in this study came from the crusts on limestone gravel and the particles attached on the algae.

The fresh synthetic Al-precipitates are X-ray amorphous. However, with ageing, diffraction peaks appeared in XRD patterns of several samples, although a major fraction of each of these samples is still amorphous or poorly crystalline. The only exception is the sample prepared from a solution consisting of $Al_2(SO_4)_3$ and KOH, which re-crystallized mostly to alunite ($KAl_3(SO_4)_2(OH)_6$) upon ageing. The ATR-FTIR spectra of gels prepared from $Al_2(SO_4)_3$ shows a distinct band at $\sim$1100 cm^{-1}, which is caused by the asymmetric stretching of sulfate. These spectra are similar to that of acidic Al–SO_4 solutions.

The X-ray microscopy studies allowed the direct investigation of the state of coagulation or dispersion of wet synthetic gels. The gels are composed of particles with poorly defined shape and dimensions. The only exception is the sample prepared from $Al_2(SO_4)_3$–KOH solutions, which primarily consists of round 5 μm plate-like particles (see Fig. 11). As mentioned before, this sample consisted mostly of alunite. The Al-NEXAFS spectra of all amorphous (based on the XRD results) gels are similar, and exhibit two maxima. Their energy and relative intensity slightly varies from sample to sample. Nevertheless, the similarity of these spectra indicates that the different anions used in the study (Cl^-, NO_3^-, SO_4^{2-}), and the different hydroxides used in titration (NaOH, KOH) have little influence on the local environment of Al. Within the uncertainty of the measurement, all aluminum is octahedrally coordinated. The measured spectra resemble the boehmite spectra measured by Ildefonse et al. [47] and Yoon et al. [35].

The Al-NEXAFS spectra of the natural Al-flocs differ significantly from the spectra of the synthetic gels. The white line is broad; and the doublet seen in the spectra of synthetic gels is poorly resolved for the natural samples (see Fig. 11). These spectral differences between the synthetic and natural samples suggest that the synthetic gels are only approximate models for the samples that exist in field settings. The influence of other factors, such as cations and anions, time, seasonal wetting and drying, should be considered when comparing the structure of natural and synthetic gels. Studies are in progress to evaluate these factors, and X-ray spectromicroscopy facilities offer unique ways to probe the chemistry of natural wet Al-gels.

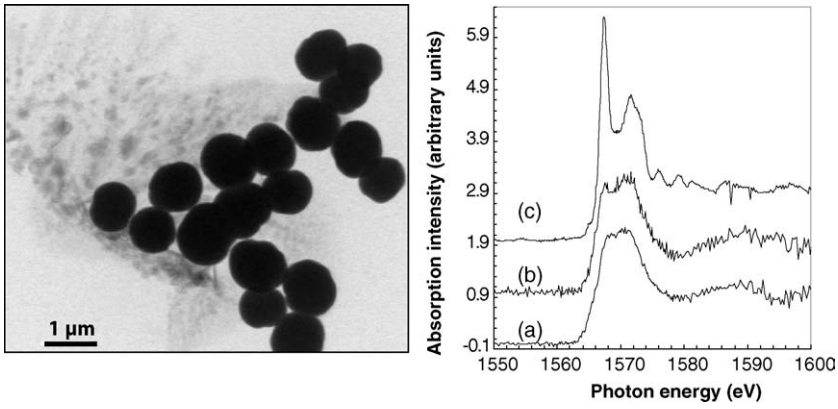

Fig. 11. Left panel: STXM image of Al-precipitates formed in the presence of K^+ and SO_4^{2-}. Right panel: Al-NEXAFS spectra of natural (a) and synthetic (b) Al-precipitates. The Al-NEXAFS spectrum of corundum (c), which exhibits octahedral-Al only, is shown for comparison.

3.6. Investigation of biofilms using STXM (A.P. Hitchcock, J.J. Dynes, T. Araki, J.R. Lawrence, G.G. Leppard, T. Tyliszczak)

In many environments modified by human activity – mining, manufacturing, vehicle exhaust, etc. – there are high concentrations of potentially hazardous metal species. Biofilms are colonies of microbial species (bacteria, algae, fungi, diatoms, etc.) linked by extracellular polymeric substances (EPS). They are ubiquitous in nature, and in some cases have been found to be surprisingly resistant to the presence of toxic metal species. This has lead to proposals to use intentional cultivation of optimized biofilms as an approach to sequestration and remediation of contaminated sites. Optimization of the culture and nutrients for such purposes requires improved understanding of the interaction of biofilms and metals in the environment. Although EPS are mainly microbial polysaccharides, other biochemical macromolecules, such as proteins, nucleic acids, and polymeric lipophilic compounds, have been identified and are suspected to play important roles in metal-biofilms interactions. EPS represent a major structural component of biofilms and are known to be responsible for sorption processes used to provide nutrients to the living entities and to help control exposure to toxic metal and organic substances [48–50]. Particularly in complex environmental systems, the EPS are difficult if not impossible to chemically map without the use of analytical microscopies. X-ray microscopy using wet cell techniques is particularly powerful since it allows measurements to be performed on fully hydrated biofilms, which are very close to the conditions of undisturbed growth. The intrinsic X-ray absorption properties of the species – both bio-macromolecules and metal compounds – are used as the analytical signal. Full field transmission X-ray microscopy (TXM) has been used for a number of studies of biological and environmental systems, such as work on early stage *Pseudomonas putida* biofilms [51]. However, existing TXM instruments have relatively limited spectroscopic capabilities. In contrast STXM, particularly on high-resolution beamlines like the ALS-MES beamline, provides the full analytical power of X-ray absorption spectroscopy. STXM has been used by Tonner and co-workers for studies on bio-generated Mn nodules and Fe minerals [52,53]. Chan et al. have used X-ray photoemission electron microscopy to investigate iron biomineralization [54].

We are using STXM on both the ALS 5.3.2 bending magnet beamline [55,56] and on the undulator 11.0.2 MES beamline to quantitate and speciate metals in natural and metal challenged riverine biofilms. The biofilm samples are grown on silicon nitride membrane windows [57] embedded on polycarbonate support plates in bioreactors at the National Water Reasearch Institute Laboratory in Saskatoon (see Fig. 12). After appropriate maturation and exposure to specific metal species, these membranes are removed from the bioreactor, capped with a second silicon nitride membrane window, sealed with silicone or epoxy to form a wet cell, transported cooled to the ALS, and recorded with as minimum a delay as possible (1–3 days, with the bioactivity suspended by reduced temperature). In most cases, the samples are exposed to fluorescent stains and confocal laser scanning microscopy (CLSM) is performed to identify specific bio-species. Identical regions of the biofilms are studied by CLSM and STXM [58,59]. STXM is used to acquire images at photon energies that highlight specific species; to acquire point spectra or linescan spectra at locations of interest; and, in the most powerful implementation, image sequences [60], which, after appropriate analysis, provide quantitative maps of the biotic and abiotic components of biofilms. We have mapped protein, nucleic acids, lipids, and polysaccharides in riverine biofilm systems [58], Ca and K in the same systems [61], and we have studied the distribution of metal species in cultivated biofilms which were exposed intentionally to low concentrations of nickel chloride [62].

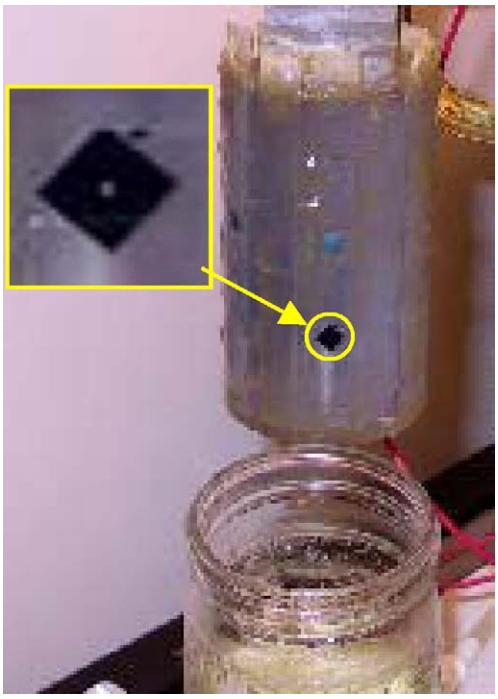

Fig. 12. Bioreactor (at NWRI, Saskatoon) used to grow biofilms under controlled conditions on silicon nitride membranes embedded in polycarbonate growth plate.

Fig. 13 illustrates our approach, as well as the complexity and diversity of these samples. Fig. 13a is a low resolution STXM image of the full (1000 μm × 800 μm) window area of the wet cell. Fig. 13b is an image of a 40 μm × 40 μm region recorded at 705 eV, just below the onset of the Fe 2p absorption. Fig. 13c is an image recorded at 708.7 eV (un-calibrated energy), at the maximum of the Fe $2p_{3/2}$ signal. Fig. 13d is the difference of these two absorption images, which provides a qualitative map of the iron distribution. The latter can be readily converted to a quantitative map as outlined elsewhere [62]. Although speciation information is at best incomplete, image differences provide a rapid way to locate regions with interesting distributions of specific species. It works best with elements having strong $p \rightarrow d$ resonances (Ca 2p, K 2p, metal 2p edges). Measurements on/off the strong C $1s \rightarrow \pi^*$ (amide) signal at 288.2 eV is very useful to map the biotic entities [61]. Once one has identified an interesting area, such as that indicated from the Fe mapping shown in Fig. 13, one can zoom in and record image sequences at high spatial resolution to speciate and quantitate the metals present.

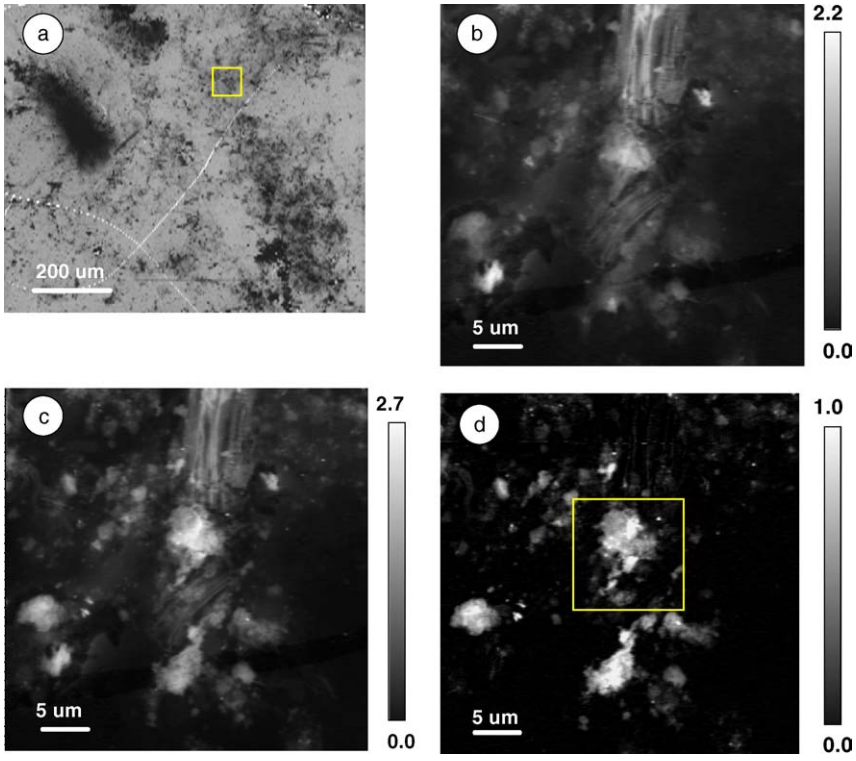

Fig. 13. (a) Overview transmission image of the full wet cell of a river water biofilm sample recorded at 288.2 eV (BL532 STXM). (b) Optical density image of the indicated (40 μm × 40 μm) region at 705 eV (MES STXM). (c) Same area at 708.7 eV. (d) Difference of (c) – (b), indicating optical density associated with absorption by iron species. They grayscale is optical density (b and c), or difference in optical density (d).

Fig. 14 presents component maps and color coded composites derived from Ca 2p, K 2p, Mn 2p, Fe 2p, and Ni 2p MES STXM measurements. Fig. 14a is an OD image at 279 eV (non-organic) of a wet river water biofilm. Several diatom skeletons dominate the landscape. Fig. 14b is a composite map where the grayscale images the bio-organic components as visualized by the difference of PD images at 288.2 eV (protein) and 279 eV (non-organic) ($I_{288.2} - I_{279}$), combined with maps of Ca ($I_{352} - I_{350}$) (green) and K ($I_{296} - I_{295}$) (blue). The K^+ and Ca^{2+} signals are highly localized in the regions of specific bacteria. Fig. 14c is an image of the Mn signal map in the region just below the vertical diatom skeleton indicated in Fig. 14b, obtained by fits of a Mn 2p image sequence to the Mn signal in Fig. 14f. Fig. 14d is a composite map of the Fe(II) and Fe(III) signals. Fig. 14e is composite map of two apparently different Ni 2p signals, which have rather similar spectra and thus may differ only in ligand environment and not oxidation state. In the case of the metal 2p signals, the reference spectra were obtained by extracting the spectra of metal-rich regions from the image sequence itself. The extracted spectra for the Mn, Fe and Ni 2p are plotted in Fig. 14f. A detailed interpretation of these results requires comparison of the characteristic spectra to those of likely mineral species [62]. Quantitative mapping and spectral comparisons [58,62] indicate that, in the region studied in detail in Fig. 14, both Fe(II) and Fe(III) species are present with partly overlapping but mostly adjacent spatial distributions, and that the Fe(II) species is likely associated with polysaccharides. The presence of large amounts of both Fe(II) and Fe(III) (and possibly mixed valence) species, complexed to organic material, suggests that the microbes were using the Fe species as an energy source via electron transfer mechanisms. The Ni originated from $NiCl_2$ added to the biofilm whereas the Mn was probably present in the original environment. The close association of the Ni with the Mn suggests a primarily chemical mechanism for its sequestration. Since the natural biofilm environments are so varied, it is important to examine a number of other metal-rich areas of similar bio-films to build a sense of the common motifs of biologically mediated deposits of this type. These results demonstrate the potential of STXM to provided detailed information relating to bio-mineralization and the accommodation of biofilms to potentially toxic metal species.

3.7. In situ characterization of aluminum-containing mineral–microorganism aqueous suspensions (T.H. Yoon, K. Benzerara, T. Tyliszczak, G.E. Brown, Jr.)

Knowledge of the identity and stability of natural colloids under hydrous conditions is essential for understanding their ability to transport pollutants in natural waters [63–65]. Due to their ubiquitous presence in the Earth's crust, aluminosilicate minerals such as clays are major components of natural inorganic colloids in many natural settings [66]. However, to our knowledge, there have been no spectroscopic or microscopic characterization studies of Al-containing colloidal systems in the presence of bulk water, mainly due to the lack of appropriate methods for probing sub-micron-sized Al-containing particles in hydrous environments.

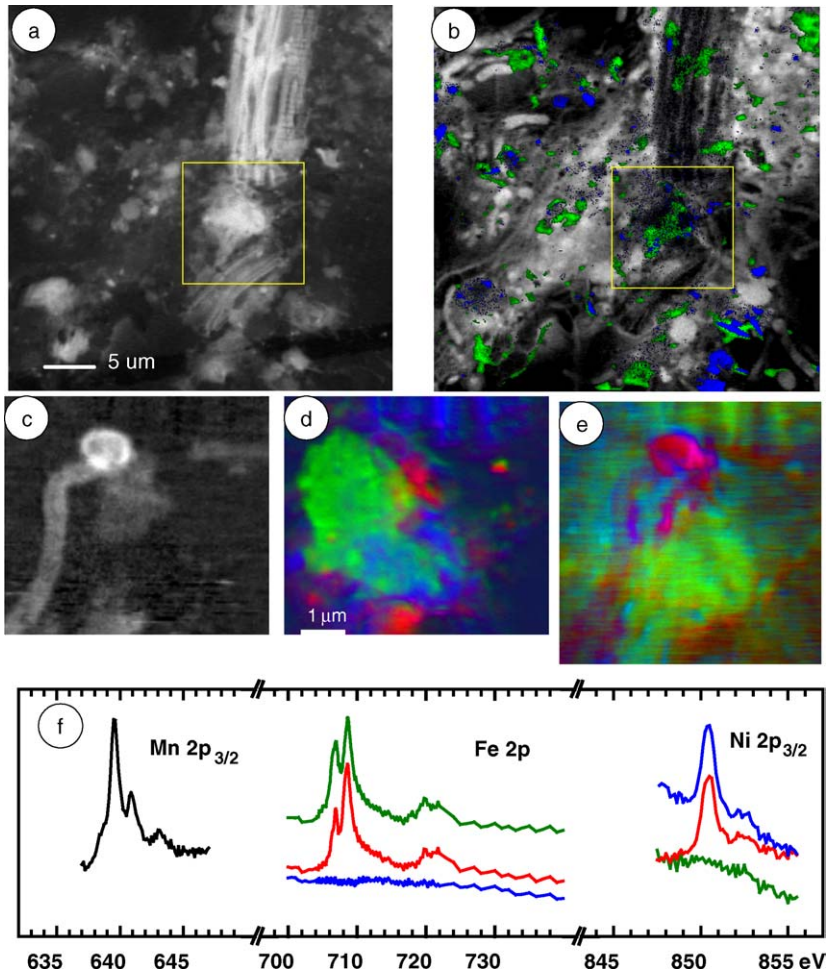

Fig. 14. (a) OD image at 279 eV (non-organic) of a wet river water biofilm. Several diatom skeletons dominate the landscape. (b) Composite map of bio-organic ($I_{288.2} - I_{279}$) (grayscale), Ca^{2+} ($I_{352} - I_{350}$) (green), and K^+ (($I_{296} - I_{295}$) (blue). (c) Mn map in indicated region. (d) composite map of Fe (III) (red), Fe (II) (green) and non-Fe (blue). (e) composite map of Ni-a (red), Ni-b (green), and non-Ni (blue). (f) Spectra extracted from image sequences and used for generating component maps contributing to parts (c–e).

We have used the MES STXM end station to investigate synthetic Al-containing mineral colloid systems, including those with bacteria and water present, as a test of its capabilities. Aqueous suspensions of Al-containing mineral mixtures (∼1 g/l for each mineral) were prepared in 0.01 M NaCl, with the pH of the solution being adjusted to 6.0 by adding 0.1 M NaOH and HCl. Approximately 1 μl of each suspension was sandwiched between two 100 nm thick silicon nitride membranes [57], which were then sealed with epoxy resin to maintain a fully hydrated environment during STXM analysis. The STXM sample chamber is He-filled to minimize attenuation of the soft X-rays. Al K-edge STXM images and NEXAFS spectra have been measured for synthetic mineral colloid mixtures under hydrous conditions and analyzed using previously collected Al K-edge NEXAFS spectra of selected reference minerals [35,67,68]. In addition, bacteria–mineral suspensions in aqueous solution have been imaged just above the carbon K-edge (E = 288.8 eV) and Al K-edge (E = 1571.6 eV) in a study of bacteria–mineral colloid interactions.

STXM images collected for a mixed aqueous suspension consisting of four finely ground Al-containing minerals [γ-Al_2O_3, corundum, boehmite (γ-AlOOH), and hydrotalcite ($Mg_6Al_2(CO_3)(OH)_{16}{\cdot}4H_2O$)] at pH 6.0 are shown in Fig. 15, which also compares STXM images collected at several different energies (A–D) and NEXAFS spectra extracted from different positions (a–e) of these image stacks.

As can be seen from Fig. 15B–D, STXM images collected at different energies can be used to distinguish different Al-containing mineral phases, especially those with different Al first coordination numbers. The image collected at E = 1565.4 eV (corresponding to the first peak of γ-Al_2O_3 NEXAFS spectrum, Fig. 15B) shows only several γ-Al_2O_3 particles (2–3 μm in diameter). As the incident X-ray energy is increased to the positions of the corundum and boehmite Al K-edges (1567.5 and 1571.8 eV, as shown in Fig. 15C and D, respectively), a large number of small particles (100–200 nm in diameter) become apparent in the mapped area. These small particles most likely consist of corundum, boehmite, and/or hydrotalcite. However, without NEXAFS spectral processing and comparison (or deconvolution) with reference spectra, it is difficult to distinguish among particles of different minerals with the same Al-

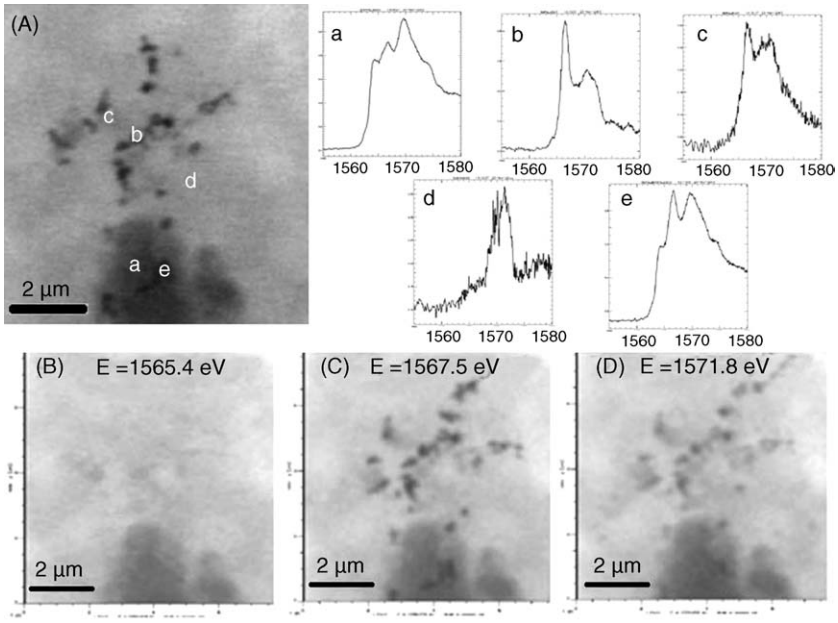

Fig. 15. STXM image and Al K-edge NEXAFS spectra of mineral particle mixtures under hydrous conditions measured at (A) $E = 1567.8$ eV, (B) $E = 1565.4$ eV (energy corresponds to the first peak of the γ-Al_2O_3 NEXAFS spectrum), (C) $E = 1567.5$ eV (energy corresponds to the first peak of the corundum NEXAFS spectrum), and (D) $E = 1571.8$ eV (energy corresponds to the third peak of the boehmite NEXAFS spectrum). Each NEXAFS spectrum was collected from areas indicated by (a–e).

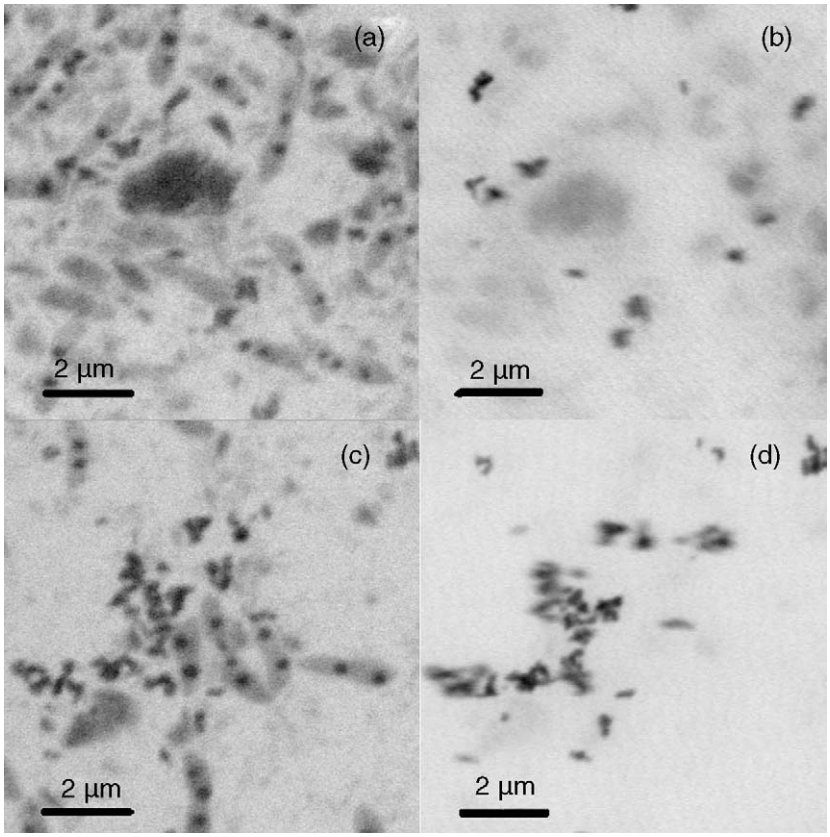

Fig. 16. STXM images of a *Caulobacter crescentus*-mineral mixture (corundum and montmorillonite) in an aqueous suspension measured in the vicinity of the carbon K-edge [$E = 288.8$ eV (a and c)] and the aluminum K-edge [$E = 1571.6$ eV (b and d)].

coordination number from the images collected at different energies alone.

Further processing of image stacks and resulting NEXAFS spectra was performed to distinguish the particles shown in Fig. 15C and D. Fig. 15A is a STXM image of the same mineral colloid mixture taken at an incident X-ray energy of 1567.8 eV. Also shown in Fig. 15 are Al K-edge NEXAFS spectra corresponding to regions 'a–e'. NEXAFS spectra from region a showed the same spectral features as those of the γ-Al_2O_3 reference material (see Ref. [35]), while the NEXAFS spectra from regions b and c are very similar to those of the corundum and boehmite reference materials, respectively [35]. Although we added the same concentrations of each reference mineral phase (1 g/l) to this colloidal suspension, hydrotalcite was rarely observed in this sample, except in the small area around 'd', as indicated by the peak maximum at 1571.4 eV. This is probably due to the relatively low aluminum content (∼9 wt%) in this mineral phase and its very fine grain size and/or its dispersed nature under the aqueous conditions utilized in our study. We also observed unusual NEXAFS features in region e, which is a composite spectrum of α-Al_2O_3 and γ-Al_2O_3, resulting from clusters of small α-Al_2O_3 particles (∼150 nm) associated with a larger γ-Al_2O_3 particle in the sample volume probed by the X-ray beam.

Fig. 16 shows STXM images obtained in situ from a prepared aqueous suspension of mineral particles [corundum and montmorillonite $(Na, Ca)_{0.3}(Al, Mg)_2Si_4O_{10}(OH)_2{\cdot}nH_2O$)] and the bacterium *Caulobacter crescentus*, which is intended to mimic the complexity of natural biocolloids. Fig. 16a and c are STXM images taken near the carbon K-edge (288.8 eV), whereas Fig. 16b and d are STXM images of the same areas taken near the aluminum K-edge (1571.6 eV). The C K-edge STXM images show rod-shaped bacteria (≈2 μm long and 0.5 μm wide) as well as sub-micron-sized dark spots within the bacteria, which are consistent with polyhydroxybutyrate (PHB) granules observed in *C. crescentus* by TEM [69]. These granules are used by the bacterium as carbon and energy reserves. In Al K-edge images (Fig. 16b and d), these bacterial components (i.e., cells and dark spots within cells) are not visible, while many dark patches observed outside the bacterial cells in Fig. 16a and c are still visible in Fig. 16b and d, suggesting that these dark patches are rich in aluminum. STXM images at the Al K-edge (see Fig. 16b and d) allow the carbonaceous particles to be distinguished from the Al-containing colloidal components. Furthermore, Al K-edge NEXAFS analyses of the dark and gray areas shown in Fig. 16b confirm that the small (<500 nm in diameter) dark clusters in Fig. 16b and d are corundum particle clusters, whereas the larger and more diffuse objects (∼2 μm in diameter) are montmorillonite particles. It is further observed in the STXM images that the bacterial cells and mineral particles are closely associated, forming relatively large bacteria–mineral flocs. Interestingly, however, the bacterial cell wall surfaces are not in direct contact with the corundum or montmorillonite particle surfaces in the aqueous solutions used in this study (pH 7, minimal growth medium). Because production of EPS and attachment to various surfaces via an adhesive holdfast organelle located at the end of the stalk has previously been observed in *C. crescentus* [70,71], we suggest that these adhesive holdfast organelles as well as EPS produced by *C. crescentus* bind the bacteria to the clay and corundum particles. The formation of EPS-mediated flocs is likely to have a significant impact on the physical stability of colloidal particles [72].

3.8. STXM study of calcium phosphate biomineralization by Caulobacter crescentus (K. Benzerara, T.H. Yoon, T. Tyliszczak, G.E. Brown, Jr.)

Calcification, i.e., the precipitation of Ca-containing minerals, is a ubiquitous process at the Earth's surface impacting global geochemistry [73] and is an important issue for human health as well, either as an essential process (e.g., bone formation [74]) or as the cause of several diseases [75]. Microbes are often associated with Ca-containing minerals in the environment, but it is usually difficult to decipher if these organisms are directly involved in the precipitation process, if they simply modify the chemistry of the medium (e.g., pH), or if specific molecules assist the precipitation and nucleation of minerals. Moreover, the relative importance in nature of proteins, polysaccharides, or lipids as potential frameworks for the precipitation of calcium-containing minerals is yet to be determined [76].

STXM proves to be well suited to study biocalcified samples, which gather diverse organic molecules and poorly crystallized nanometer-sized minerals. Such samples are difficult to study by other techniques like transmission electron microscopy, for example. In a recent study [77], we showed that the Ca $L_{2,3}$-edges for hydroxyapatite [$Ca_5(PO_4)_3OH$)], calcite ($CaCO_3$), vaterite (μ-$CaCO_3$), and aragonite ($CaCO_3$) are unique and can be used as probes to detect these different mineral phases (data not shown), which are the most common in biomineralizing systems. We then used high spatial and energy resolution NEXAFS spectra at the C K-edge and the Ca $L_{2,3}$-edge on *Caulobacter crescentus* cells biomineralized under laboratory conditions. Fig. 17a shows *C. crescentus* cells incubated for 3 weeks in a growth medium supplemented with calcium. *C. crescentus* cells are kidney bean-shaped of dimensions 2 μm long and 0.7 μm wide (Fig. 17a). The Ca map shows that Ca is distributed throughout the cells (Fig. 17b). The Ca concentration is estimated to be 10^{-14} g μm^{-2} in the cells depicted in Fig. 17c and is up to 10^{-13} g μm^{-2} in more mineralized cells. The Ca $L_{2,3}$-edge NEXAFS spectra measured on different cells were identical and characteristic of hydroxyapatite (Fig. 17e). This study, like several previous ones [78], unambiguously shows that calcium phosphate precipitation occurs on or inside the cells.

The C K-edge spectra were measured on the same cells and display at least five peaks (Fig. 17d). Using the reference spectra of Lawrence et al. [58], these peaks can be assigned to different C-containing functional groups. The peak at 285.2 eV is related to aromatic groups in proteins [79]. The peaks at 286.8 and 288.2 eV likely correspond to phenolic groups and/or ketonic groups [80] and to amide carbonyl groups in proteins, respectively. The peak at 289.5 eV is at the same energy position as that of the C=O groups in nucleic acids. Finally, the peak at 290.3 eV was observed only in *C. crescentus* cultured in a growth medium supplemented with calcium and is indicative of carbon-

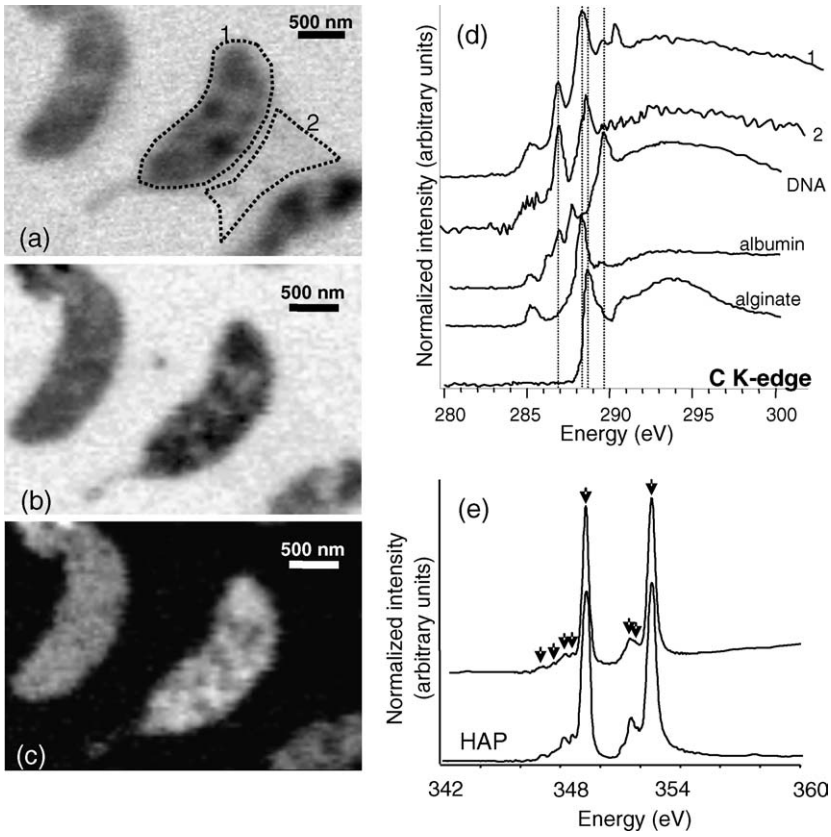

Fig. 17. Spectromicroscopy on *C. crescentus* incubated for 3 weeks in calcium-rich growth medium at the calcium $L_{2,3}$-edge. (a) STXM image taken at 288.2 eV showing the kidney bean-shaped cells. (b) STXM image of the same area at 349.3 eV (Ca L_2 edge). (c) Calcium map showing the calcium enrichment of cells. (d) Carbon K-edge NEXAFS spectra of a *C. crescentus* cell (spectrum 1), and the EPS (spectrum 2) resulting from the image stack on the area depicted in (a). Reference spectra [58] of DNA, albumin (taken as a model for protein), and alginate (taken as a model for acidic polysaccharides) are shown for comparison. (e) Calcium $L_{2,3}$-edge NEXAFS spectra of a *C. crescentus* cell shown in (b). The spectra were identical for all the areas tested. Peak positions were 347.1, 347.7, 348.2, 348.6, 349.3, 351.5, and 352.6. A reference hydroxyapatite calcium $L_{2,3}$-edge NEXAFS spectrum is shown for comparison and displays the same peaks (see arrows).

ate groups, which are incorporated into hydroxyapatite structure. A C-containing polymeric material bridging between two cells can be seen in Fig. 17a. The C K-edge NEXAFS spectrum from this area shows a peak at 288.5 eV, which corresponds to carboxylic groups in polysaccharides. This extracellular polymer thus likely corresponds to EPS, which has been shown to be produced by this strain [71]. No carbonate peak was observed in this area. The ability of STXM to characterize the speciation of carbon in mineralized cells provides a unique signature for microorganisms versus simple macromolecules like proteins or polysaccharides and brings new insight to the fate of organic compounds at a single-cell scale during the biomineralization process, showing that proteins, polysaccharides, and nucleic acids are still detected in mineralized cells. Moreover, STXM may be a unique technique for detecting unambiguous evidence of ancient life in rocks.

3.9. Iron oxidation at a microorganism–mineral interface (K. Benzerara, T.H. Yoon, T. Tyliszczak, G.E. Brown, Jr.)

The role of microorganisms in the dissolution of silicates and in the cycling of Fe has been the focus of many experimental studies [81], some of which have shown that microorganisms can radically modify the dissolution rates of Fe-silicates. They are thought to do so by creating microenvironments in which pH and other solution variables can dramatically differ from bulk conditions [82,83]. The pathways of microbially mediated Fe-silicate dissolution reactions in nature remain, however, largely unexplored, particularly at the nanometer scale. We have used STXM, coupled with transmission electron microscopy, to examine bioweathering products on an Fe–Mg-silicate (orthopyroxene) colonized by a microorganism and exposed at the Earth's surface for 70 years. The microorganism is in contact with the orthopyroxene and is bordered by a cluster of nanometer-sized rod-shaped calcite single crystals (Fig. 18a). Using an ultra-thin (80 nm) cross-section through the microorganism, the calcite crystals and the pyroxene STXM was used to perform NEXAFS spectroscopy at the Fe L_3-edge [84], which allowed us to determine the Fe oxidation state [85] in the microorganism–calcite–pyroxene microcosm (Fig. 18b and c). Iron spectra taken on the pyroxene (area 1) showed a major peak at 707.8 eV, indicative of Fe^{2+} (Fig. 18c). Iron-rich particles in the calcite cluster (area 2) displayed a major peak at 709.5 eV, which indicates that iron was oxidized after its release by dissolution of the pyroxene (Fig. 18c). In the microorganism (area 3), however, the Fe L_3-edge shows a mixed iron valence (Fe^{2+} and Fe^{3+}) (Fig. 18c). One possible explanation for heterogeneous iron valence is that this microorganism creates a special

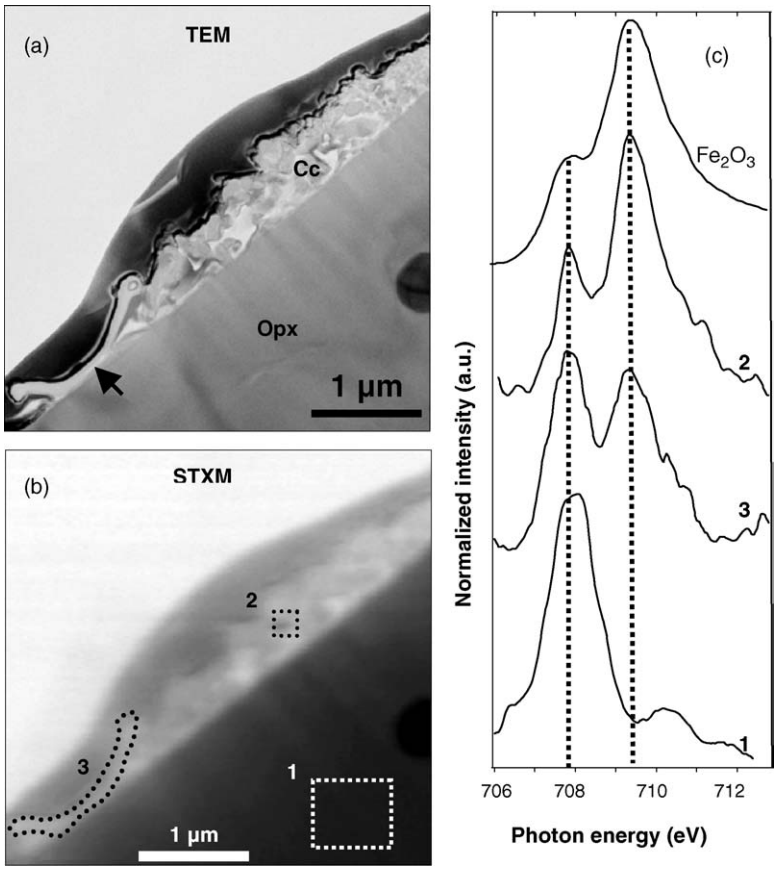

Fig. 18. (a) TEM image of a cross-section showing the microorganism (arrow), the calcite crystal cluster (Cc), and the pyroxene (Opx). (b) Equivalent STXM image at 707.8 eV. (c) Iron L_3-edge NEXAFS spectra from the pyroxene (area 1), the calcite cluster (area 2), the microorganism (area 3), and reference hematite, representing the Fe^{3+} endmember. Dashed lines represent the positions of Fe L_3 maxima for Fe^{2+} and Fe^{3+} at 707.8 and 709.5 eV, respectively.

microenvironment with a particular pO_2, and/or modifies the pH, resulting in slower oxidation of iron. Another possibility is that organic molecules produced by the microorganism strongly bind dissolved Fe^{2+} and thus inhibit its oxidation. Whatever mechanisms are involved in iron redox behavior, the microorganism heavily impacts iron oxidation in a microenvironment, resulting in a likely major modification of pyroxene reactivity compared with a purely abiotic environment. This study provides unambiguous evidence for the existence of nanoenvironments created by a microorganism. Such nanoenvironments have been suggested by a number of previous studies but have not been confirmed in this way.

4. Summary

Through brief descriptions of the experimental capabilities and several diverse examples we have demonstrated that the ALS-MES soft X-ray beamline (11.0.2) is a powerful tool with particular strength for the investigation of environmentally relevant materials under realistic conditions. STXM is capable of providing molecular-level information on the speciation and phase association of samples at low concentrations, under wet conditions and with a spatial resolution of 25 nm. Due to the small amounts of material that are needed in STXM experiments, it is also a valuable tool for the investigation of radioactive samples. Ambient pressure PES compliments the more bulk-sensitive techniques (XES, STXM) since it is an excellent method for the investigation of liquid/vapor and solid/vapor interfaces at Torr pressures. Combined, the three dedicated end stations at the ALS-MES beamline provide the opportunity to study a wide variety of samples under different conditions, from well-defined single crystal surfaces in ultra-high vacuum to bacteria in aqueous environments.

Acknowledgements

This research, the ALS, and the ALS-MES beamline 11.0.2 are supported by the Director, Office of Science, Office of Basic Energy Sciences, Division of Chemical Sciences, Geosciences, and Biosciences and Materials Sciences Division of the U.S. Department of Energy at the Lawrence Berkeley National Laboratory under Contract No. DE-AC03-76SF00098 (TT, MKG, DKS, HB). HB, DFO and MS would like to thank K. Ihmann, E. Kleimenov, M. Hävecker, A. Knop-Gericke, and R. Schlögl (Fritz Haber Institute of the Max Planck Society, Berlin, Germany) for the their support during the design and construction of the ambient pressure PES instrument. TT and DKS are grateful to Brian S. Fairchild of LBNL EH&S for his assistance in the performance of the actinide STXM experiments. GEB and THY gratefully acknowledge the support of NSF Grants

CHE-0089215 (Stanford University CRAEMS on Chemical and Microbial Interactions at Environmental Interfaces) and CHE-0431425 (Stanford Environmental Molecular Science Institute) as well as NSF Grant EAR-9905755 (GEB and KB). KB also acknowledges partial support from a Lavoisier Fellowship from the French Foreign Ministry. GEB, KB and THY thank Sirine Fakra for her assistance during STXM experiments, and Jeffrey Catalano (Stanford University) for providing clay minerals used in these experiments. JCH, MS, GK, DFO, and SG thank the NSF for support (grants 0080806, 0209719, and 0431312) and acknowledge the support by the Director, Office of Science, Office of Basic Energy Sciences under Contract No. DE-AC03-76SD00098. GK thanks the Alexander von Humboldt Foundation for support. APH, JJD, JRL, and GGL acknowledge the support of the National Water Research Institute, Environment Canada, the Advanced Food and Materials Network, NSERC (Canada), and the Canada Research Chair program (APH). AN, HO, and KA acknowledge supported by NSF grants CHE-0089215 and CHE-0431425, the Swedish Foundation for Strategic Research, the Swedish Natural Science Research Council and the U.S. Department of Energy, Office of Basic Energy Sciences through the Stanford Synchrotron Radiation Laboratory and the Advanced Light Source. SCBM and JM would like to acknowledge NSF grants CHE-0089215 (CRAEMS) and CHE-0431425 (EMSI), and Princeton University's Hess Post-Doctoral Fellowship Program.

References

[1] G.E. Brown Jr., V.E. Henrich, W.H. Casey, D.L. Clark, C. Eggleston, A. Felmy, D.W. Goodman, D.W. Grätzel, G. Maciel, M.I. McCarthy, K. Nealson, D.A. Sverjensky, M.F. Toney, J.M. Zachara, Chem. Rev. 99 (1999) 77.
[2] P.A. Thiel, T.E. Madey, Surf. Sci. Rep. 7 (1987) 211.
[3] M.A. Henderson, Surf. Sci. Rep. 46 (2002) 1.
[4] T. Tyliszczak, T. Warwick, A.L.D. Kilcoyne, S. Fakra, D.K. Shuh, T.H. Yoon, G.E. Brown Jr., S. Andrews, V. Chembrolu, J. Strachan, Y. Acreman, Synchrotron Radiation Instrumentation 2003 AIP Conference Proceedings 705, 2004, p. 1356.
[5] J. Stöhr, NEXAFS Spectroscopy, Springer, Berlin, 1992.
[6] A. Nilsson, L.G.M. Pettersson, Surf. Sci. Rep. 55 (2004) 49.
[7] D.F. Ogletree, H. Bluhm, G. Lebedev, C.S. Fadley, Z. Hussain, M. Salmeron, Rev. Sci. Instrum. 73 (2002) 3872.
[8] H. Ogasawara, B. Brena, D. Nordlund, M. Nyberg, A. Pelmenschikov, L.G.M. Pettersson, A. Nilsson, Phys. Rev. Lett. 89 (2002) 276102.
[9] T. Warwick, N. Andresen, J. Comins, K. Kaznacheyev, J.B. Kortright, J.P. McKean, H.A. Padmore, D.K. Shuh, T. Stevens, T. Tyliszczak, Synchrotron Radiation Instrumentation 2003 AIP Conference Proceedings, vol. 705, 2004, p. 458.
[10] H. Petersen, Optics Comm. 40 (1982) 402.
[11] R. Follath, F. Senf, Nucl. Instrum. Methods Phys. Res. A390 (1997) 388.
[12] D.F. Ogletree, H. Bluhm, in preparation.
[13] Y.-D. Chuang, B. Mesler, J. Pepper, W. McKinney, Z. Hussain, E. Gullikson, J. Underwood, P. Batson, D.K. Shuh, T. Toliszczak, D. Qian, M.Z. Hasan, J. Phys. Chem. Solids, submitted for publication.
[14] C.F. Hague, J.H. Underwood, A. Avila, R. Delaunay, H. Ringuenet, M. Marsi, M. Sacchi, Rev. Sci. Instrum. 76 (2005) 023110.
[15] A. Nilsson, M. Weinelt, T. Wiell, P. Bennich, O. Karis, N. Wassdahl, J. Stöhr, M. Samant, Phys. Rev. Lett. 78 (1997) 2817.
[16] J. Hasselström, O. Karis, M. Nyberg, L.G.M. Pettersson, M. Weinelt, N. Wassdahl, A. Nilsson, J. Phys. Chem. B 104 (2000) 11480.
[17] K. Andersson, A. Nikitin, L.G.M. Pettersson, A. Nilsson, H. Ogasawara, Phys. Rev. Lett. 93 (2004) 196101.
[18] L. Onsager, N.N.T. Samaras, J. Phys. Chem. 2 (1934) 528.
[19] J.H. Hu, Q. Shi, P. Davidovits, D.R. Worsnop, M.S. Zahniser, C.E. Kolb, J. Phys. Chem. 99 (1995) 8768.
[20] E.M. Knipping, M.J. Lakin, K.L. Foster, P. Jungwirth, D.J. Tobias, R.B. Gerber, D. Dabdub, B.J. Finlayson-Pitts, Science 288 (2000) 301.
[21] D. Liu, G. Ma, L.M. Levering, H.C. Allen, J. Phys. Chem. B 108 (2004) 2252.
[22] E.A. Raymond, G.L. Richmond, J. Phys. Chem. B 108 (2004) 5051.
[23] P.B. Petersen, J.C. Johnson, K.P. Knutsen, R.J. Saykally, Chem. Phys. Lett. 397 (2004) 46.
[24] P. Jungwirth, D.J. Tobias, J. Phys. Chem. B 105 (2001) 10468.
[25] P. Jungwirth, D.J. Tobias, J. Phys. Chem. B 106 (2002) 6361.
[26] S. Holmberg, Z.C. Yuan, R. Moberg, H. Siegbahn, J. Electron Spectrosc. Relat. Phenom. 47 (1988) 27.
[27] R. Moberg, F. Bökman, O. Bohman, H.O.G. Siegbahn, J. Chem. Phys. 94 (1991) 5226.
[28] O. Baschenko, F. Bökman, O. Bohman, H.O.G. Siegbahn, J. Electron Spectrosc. Relat. Phenom. 62 (1993) 317.
[29] S. Ghosal, J.C. Hemminger, H. Bluhm, B.S. Mun, E.L.D. Hebenstreit, G. Ketteler, D.F. Ogletree, F.G. Requejo, M. Salmeron, Science 307 (2005) 563.
[30] J.J. Yeh, I. Lindau, At. Data Nucl. Data Tables 32 (1985) 1.
[31] W.F. Linke, Solubilities, Inorganic and Metal Organic Compounds: A Compilation of Solubility Data from the Periodical Literature, vol. 2, fourth ed., Van Nostrand, Princeton, NJ, 1958.
[32] J.D. Denlinger, E. Rotenberg, T. Warwick, G. Visser, J. Nordgren, J.-H. Guo, P. Skytt, S.D. Kevan, K.S. McCutcheon, J.G. Tobin, D.K. Shuh, J.J. Bucher, N.M. Edelstein, B.P. Tonner, Rev. Sci. Instrum. 66 (1995) 1342.
[33] J. Terry, R.K. Schulze, J. Lashley, J.D. Farr, T. Zocco, K. Heinzelman, E. Rotenberg, D.K. Shuh, G. Van der Laan, J.G. Tobin, Surf. Sci. 499 (2002) 141.
[34] D.K. Shuh, S.M. Butorin, J.-H. Guo, J. Nordgren, Mater. Res. Soc. Symp. Proc. 802 (2004) 131.
[35] T.H. Yoon, S.B. Johnson, C.S. Doyle, K. Benzerara, T. Tyliszczak, D.K. Shuh, G.E. Brown Jr., Langmuir 20 (2004) 10361.
[36] E. Browne, R.B. Firestone, in: V.S. Shirley (Ed.), Table of Radioactive Isotopes, John Wiley & Sons, New York, 1986, pp. C14–C16.
[37] T. Tyliszczak, H.J. Nilsson, P. Nachimuthu, D.K. Shuh, 2004, unpublished results.
[38] S. Sharmasarkar, S.J. Traina, T. Tyliszczak, H.J. Nilsson, D.K. Shuh, in press.
[39] Actinide Oxides, Actinide Research Quarterly, Nuclear Materials Technology, Los Alamos National Laboratory, 2nd Quarter, 2004.
[40] F. Jollet, T. Petit, S. Gota, N. Thromat, M. Gautier-Soyer, A. Pasturel, J. Phys. Cond. Matter. 9 (1997) 9393.
[41] K.E. Ivanov, S.M. Butorin, J.-H. Guo, D.K. Shuh, unpublished results.
[42] G.W. Brindley, D.L. Bish, Nature 263 (1976) 353.
[43] B.C. Koch, H.C.B. Hansen, 16th World Congress of Soil Science, Montpellier, Proceedings, France, August 20–26, 1998, pp. 1–9 (Provided on CD reg. #1907).
[44] A. Violante, P. Violante, Clays Clay Miner. 28 (1980) 425.
[45] P.H. Hsu, Clays Clay Miner. 36 (1988) 25.
[46] G. Furrer, B.L. Phillips, K. Ulrich, R. Pöthig, W.H. Casey, Science 297 (2002) 2245.
[47] Ph. Ildefonse, D. Cabaret, Ph. Sainctavit, G. Calas, A.-M. Flank, P. Lagarde, Phys. Chem. Miner. 25 (1998) 112.
[48] M.J. Brown, J.N. Lester, Water Res. 16 (1982) 1539.
[49] M.W. Mittelman, G.G. Geesey, Appl. Environ. Microbiol. 49 (1985) 846.
[50] H. Lünsdorf, I. Brümmer, K.N. Timmis, I. Wagner-Döbler, J. Bacteriol. 179 (1997) 31.
[51] E.S. Gilbert, A. Khlebnikov, W. Meyer-Ilse, J.D. Keasling, Water Sci. Technol. 39 (1999) 269.

[52] B.P. Tonner, T. Droubay, J. Denlinger, W. Meyer-Ilse, T. Warwick, J. Rothe, E. Kneedler, K. Pecher, K. Nealson, T. Grundl, Surf. Interface Anal. 27 (1999) 247.
[53] K.H. Pecher, D.M. McCubbery, E.M. Kneedler, J. Rothe, J.R. Bargar, G. Meigs, L. Cox, K.H. Nealson, B.P. Tonner, Geochim. Cosmochim. Acta 67 (2003) 1089.
[54] C.S. Chan, G. De Stasio, S.A. Welch, M. Girasole, B.H. Frazer, M.V. Nesterova, S. Fakra, J.F. Banfeld, Science 303 (2004) 1656.
[55] T. Warwick, H. Ade, A.L.D. Kilcoyne, M. Kritscher, T. Tylisczcak, S. Fakra, A.P. Hitchcock, P. Hitchcock, H.A. Padmore, J. Synchrotron Radiat. 9 (2002) 254.
[56] A.L.D. Kilcoyne, T. Tyliszczak, W.F. Steele, S. Fakra, P. Hitchcock, K. Franck, E. Anderson, B. Harteneck, E.G. Rightor, G.E. Mitchell, A.P. Hitchcock, L. Yang, T. Warwick, H. Ade, J. Synchrotron Radiat. 10 (2003) 125.
[57] Silson, Ltd., Northampton, United Kingdom.
[58] J.R. Lawrence, G.D.W. Swerhone, G.G. Leppard, T. Araki, X. Zhang, M.M. West, A.P. Hitchcock, Appl. Environ. Microbiol. 69 (2003) 5543.
[59] J.R. Lawrence, A.P. Hitchcock, G.G. Leppard, T.R. Neu, in: I.G. Droppo, G.G. Leppard, T.M. Milligan, S.N. Liss (Eds.), CRC Press, in press.
[60] C. Jacobsen, S. Wirick, G. Flynn, C. Zimba, J. Microscopy 197 (2000) 173.
[61] A.P. Hitchcock, C. Morin, X. Zhang, T. Araki, J. Dynes, H. Stöver, J. Brash, J.R. Lawrence, G.G. Leppard, J. Electron Spectrosc. Relat. Phenom. 144–147 (2005) 259.
[62] J.J. Dynes, T. Tyliszczak, T. Araki, J.R. Lawrence, G.D.W. Swerhone, G.G. Leppard, M.M. West, A.P. Hitchcock, Geochim. Cosmochim. Acta, in preparation.
[63] J.F. McCarthy, J.M. Zachara, Environ. Sci. Technol. 23 (1989) 496.
[64] O. Gustafsson, P.M. Gschwend, Limnol. Oceanogr. 42 (1997) 519.
[65] D. Grolimund, M. Borkovec, K. Barmettler, H. Sticher, Environ. Sci. Technol. 30 (1996) 3118.
[66] J. Buffle, K.J. Wilkinson, S. Stoll, M. Filella, J.W. Zhang, Environ. Sci. Technol. 32 (1998) 2887.
[67] C.S. Doyle, S.J. Traina, H. Ruppert, T. Kendelewicz, J.J. Rehr, G.E. Brown Jr., J. Synchrotron Radiat. 6 (1999) 621–623.
[68] G.E. Brown Jr., F.D. Dikman, G.A. Waychunas, SSRL Rep. 83/01 (1983) 148.
[69] J.S. Poindexter, K.P. Pujara, J.T. Staley, Appl. Environ. Microbiol. 66 (2000) 4105.
[70] N. Ravenscroft, S.G. Walker, G.G.S. Dutton, J. Smit, J. Bact. 173 (1991) 5677.
[71] R.I. Merker, J. Smit, Appl. Environ. Microbiol. 54 (1988) 2078.
[72] Y. Liu, H.H.P. Fang, Crit. Rev. Environ. Sci. Technol. 33 (2003) 237.
[73] G.A. Zavarzin, Microbiology 71 (2002) 1.
[74] J.J. Ghidoni, Ann. Thoracic Surg. 77 (2004) 704.
[75] J.C. Elliott, Rev. Miner. Geochem. 48 (2002) 427.
[76] A. Veis, Rev. Miner. Geochem. 54 (2003) 249.
[77] K. Benzerara, T.H. Yoon, C.S. Doyle, T. Tyliszczak, B. Constantz, A.M. Spormann, G.E. Brown Jr., Proc. Nat. Acad. Sci. U.S.A. 102 (2005) 979.
[78] K. Benzerara, N. Menguy, F. Guyot, F. Skouri-Panet, G. DeLuca, M. Barakat, H. Heulin, Earth Planet. Sci. Lett. 228 (2004) 439.
[79] K. Kaznacheyev, A. Osanna, C. Jacobsen, O. Plashkevych, O. Vahtras, H. Agren, J. Phys. Chem. A 106 (2002) 3153.
[80] S.C.B. Myneni, Rev. Miner. Geochem. 49 (2002) 485.
[81] S.L. Brantley, L.J. Liermann, R.L. Guynn, A. Anbar, G.A. Icopini, J. Barling, Geochim. Cosmochim. Acta 68 (2004) 3189.
[82] W.W. Barker, S.A. Welch, J.F. Banfield, Rev. Miner. 35 (1997) 391.
[83] B.J. Little, P.A. Wagner, Z. Lewandowski, Rev. Miner. 35 (1995) 123.
[84] G. Peng, J. Van Elp, H. Jang, L. Que, W.H. Armstrong, S.P. Cramer, J. Am. Chem. Soc. 117 (1995) 2515.
[85] K. Benzerara, T.H. Yoon, N. Menguy, T. Tyliszczak, G.E. Brown Jr., Geobiology 2 (2004) 249.